Research article

Integrative analysis identified two subtypes and a taurine-related signature to predict the prognosis and efficacy of immunotherapy in hepatocellular carcinoma

Qingsong Lu [a,b,c,d,e,f,1], Yu Lou [a,b,c,d,e,f,1], Xiaozhen Zhang [a,b,c,d,e,f,1], Hanshen Yang [a,b,c,d,e,f], Yan Chen [a,b,c,d,e,f], Hanjia Zhang [a,b,c,d,e,f], Tingbo Liang [a,b,c,d,e,f], Xueli Bai [a,b,c,d,e,f,*]

a Department of Hepatobiliary and Pancreatic Surgery, the First Affiliated Hospital, School of Medicine, Zhejiang University, Hangzhou, Zhejiang, China
b Zhejiang Provincial Key Laboratory of Pancreatic Disease, the First Affiliated Hospital, School of Medicine, Zhejiang University, Hangzhou, Zhejiang, China
c Zhejiang Provincial Innovation Center for the Study of Pancreatic Diseases, Zhejiang University, Hangzhou, Zhejiang, China
d Zhejiang Provincial Clinical Research Center for the Study of Hepatobiliary & Pancreatic Diseases, Zhejiang University, Hangzhou, China
e Cancer Center, Zhejiang University, Hangzhou, China
f Research Center for Healthcare Data Science, Zhejiang Lab, Hangzhou, Zhejiang China

ABSTRACT

Hepatocellular carcinoma (HCC) is one of the most prevalent subtypes of primary liver cancer, with high mortality and poor prognosis. Immunotherapy has revolutionized treatment strategies for many cancers. However, only a subset of patients with HCC achieve satisfactory benefits from immunotherapy. Therefore, a reliable biomarker that could predict the prognosis and immunotherapy response in patients with HCC is urgently needed. Taurine plays an important role in many physiological processes. However, its participation in the occurrence and progression of liver cancer and regulation of the composition and function of various components of the immune microenvironment remains elusive. In this study, we identified and validated two heterogeneous subtypes of HCC with different taurine metabolic profiles, presenting distinct genomic features, clinicopathological characteristics, and immune landscapes, using multiple bulk transcriptome datasets. Subsequently, we constructed a risk model based on genes related to taurine metabolism to assess the prognosis, immune cell infiltration, immunotherapy response, and drug sensitivity of patients with HCC. The risk model was validated

using several independent external cohorts and showed a robust predictive performance. In addition, we evaluated the expression patterns of taurine metabolism-related genes in the tumor microenvironment and the heterogeneity of taurine metabolism among cancer cells using a single-cell transcriptome. In conclusion, our study provides insights into the important role played by taurine metabolism in tumor progression and immune regulation. Furthermore, the risk model can serve as a biomarker to assess patient prognosis and immunotherapy response, potentially helping clinicians make more precise and personalized clinical decisions.

1. Introduction

Primary liver cancer is the sixth most common malignant tumor and the third leading cause of cancer-related death worldwide. Hepatocellular carcinoma (HCC) is the most common histological subtype and comprises 75–85% of cases [1,2]. Despite inspiring advances in early diagnosis and various treatments, such as radiotherapy, chemotherapy, and systemic therapy, which are available to reduce the mortality of liver cancer, the 5-year survival rate of HCC remains unsatisfactory, at less than 18% [1]. Recently, immunotherapy, especially immune checkpoint blockade (ICB) therapy, has emerged as one of the most promising therapeutic strategies [3]. Unlike traditional cancer treatments, ICB targets immune checkpoints, such as programmed cell death 1 (PD-1) and its ligand 1 (PD-L1, also known as B7-H1), to suppress the immune evasion of tumor cells to boost antitumor immunity [4]. Clinical studies showed that the combination of ipilimumab and nivolumab could significantly improve the objective response rate (ORR) to approximately 40% in patients with metastatic melanoma [5]. However, recent studies showed that patients with HCC have a low ORR to immunotherapy, which greatly limits the clinical application of ICB in HCC [6]. Metabolic reprogramming is an important hallmark of cancer [7]. Tumor cells exhibit distinct metabolic phenotypes that profoundly influence the tumor microenvironment (TME) and the effectiveness of immunotherapy [8]. Therefore, exploring the characteristics of energy metabolism in the TME and identifying metabolic targets has become a potential strategy to enhance the efficacy of immunotherapy.

Taurine (2-aminoethyl sulfonic acid) is the most abundant free amino acid in mammalian tissues [9]. As the downstream metabolite of methionine and cysteine, taurine is widely distributed in all tissues and organs of the human body, with the highest content in the liver. Previous studies showed that taurine exerts many important physiological functions, such as anti-oxidative stress, maintenance of energy metabolism homeostasis, and anti-inflammatory processes [10,11]. A recent study revealed that taurine can inhibit tumor growth, induce tumor cell apoptosis, and mitigate the side effects of cancer chemotherapy [12]. Other studies revealed that taurine can regulate the functions of various immune cells. For example, it can promote the proliferation of T cells and B cells, reduce the activation-induced apoptosis of T cells, and antagonize macrophage M1 polarization [13–15]. Furthermore, a recent study showed that taurine combined with anti-PD1 antibodies significantly enhanced the antitumor efficacy in a mouse tumor model, indicating the potential role of taurine in cancer immunotherapy [16]. However, studies confirmed that the serum taurine level is decreased compared with normal controls in a variety of cancers, including HCC, endometrial cancer, and breast cancer [17,18], Furthermore, the serum taurine level is lower in advanced HCC compared with that in early stage HCC. These findings suggest that taurine metabolism might play an important role in the regulation of cancer cell phenotypes and the function of various components of the TME. Therefore, it is an attractive strategy to construct a prognostic signature based on taurine metabolism-related genes (TRGs) to predict the clinical outcomes and efficacy of immunotherapy in HCC.

In this study, we first evaluated the expression of TRGs in normal and cancerous tissues using bulk transcriptomes. Based on the identified differentially expressed genes (DEGs), 371 patients with HCC from The Cancer Genome Atlas (TCGA) and 243 patients from the International Cancer Genome Consortium (ICGC) were divided into two subtypes using a consensus clustering algorithm. Next, we evaluated the clinical outcomes, immune cell infiltration, and the activity of the oncogenic pathways in each subtype. Subsequently, a taurine-related risk score prognostic model for patients with HCC based on five key genes that was screened out using the least absolute shrinkage and selection operator (LASSO) Cox regression model was constructed to assess the prognosis, efficacy of immunotherapy, and sensitivity to chemotherapy drugs of HCC. The model was then verified on multiple HCC clinical cohorts treated with immunotherapy and chemotherapy. Then, at single-cell resolution, we explored the expression of TRGs in the TME and investigated the cell-cell communication between cell subsets with different metabolic activities. Thereafter, subgroups of epithelial cells were further extracted and clustered using a non-negative matrix factorization (NMF) algorithm. We evaluated pathway activity and epithelial malignancy in different subpopulations. Finally, we used transcriptional trajectory analysis to explore TRG expression and pathway activity in different cell transcriptional states.

2. Materials and methods

2.1. Data acquisition and preprocessing

Publicly available bulk transcriptome sequencing data, somatic mutation profile, and clinical information of patients with HCC were obtained from multiple data repositories, including the TCGA database [19] (TCGA-Liver Hepatocellular Carcinoma (LIHC) cohort, https://portal.gdc.cancer.gov/), the ICGC database [20] (ICGC-LIRI-JP cohort (Japanese liver cancer), https://dcc.icgc.org), and the Gene Expression Omnibus (GEO) database [21] (GSE14520, GSE76247, https://www.ncbi.nlm.nih.gov/). Transcriptome data from 110 normal liver tissues were downloaded from the UCSC Xena database (https://xenabrowser.net/). Immunotherapy data were obtained from the IMvigor210 cohort [22] and the Tumor Immunotherapy Gene Expression Resource (TIGER) database [23] (GBM-PRJNA482620, Melanoma-GSE78220, Melanoma-GSE91061, Melanoma-phs000452, Melanoma-PRJEB23709, RCC-Braun_2020, http://tiger.canceromics. org/). Chemotherapy cohorts from the TCGA database (TCGA-cell carcinoma and endocervical adenocarcinoma (CESC) cohort) and the GEO database (GSE20194, GSE28702, GSE109211, GSE50948). Single-cell data was obtained from the GEO database (GSE166635).

2.2. Collection of TRGs

The predefined taurine metabolism-related gene sets were collected from the Molecular Signatures Database (MSigDB, https://www.gsea-msigdb.org/gsea/msigdb/index.jsp), including Gene Ontology Biological Process (GOBP) taurine transport and Kyoto Encyclopedia of Genes and Genomes (KEGG) taurine and hypotaurine metabolism. Seventeen genes in the two pathways served as TRGs.

2.3. Identification of differentially expressed TRGs

After downloading and scaling TPM format data with log (TPM+1) transformation, gene expression was normalized using the "normalizeBetweenArrays" function in "limma". Additionally, to address potential batch effects in our analysis of 574 transcriptome samples, we employed the "ComBat" function from "sva" R package. [24]. Then,

principal component analysis (PCA) was performed to investigate the separation between tumor and normal tissues based on the expression data of TRGs. Finally, to identify important TRGs in HCC, differential expression analysis was conducted on 160 normal samples (50 from TCGA-LIHC and 110 from the UCSC Xena database) and 374 patients with HCC in the TCGA-LIHC cohort using the "limma" package in R software. (V 4.2.2).

2.4. Somatic mutation and copy number alteration analysis

We accessed mutation and somatic copy number alteration (CNA) data from the TCGA database using the "TCGAbiolinks" R package to investigate whether TRG mutations or CNAs affect the expression of the TRGs and the clinicopathological features of patients with HCC. Using the "maftools" R package [25], mutation annotation format (MAF) data was processed, and the "oncoplot" function was used to plot TRG mutation frequency and type. In addition, the mutation structure of the top three TRGs with the highest mutation frequency was generated using the "lollipopPlot" function. CNA and mRNA expression data of 353 patients with HCC from the TCGA-LIHC cohort were downloaded from the cbioportal database (https://www.cbioportal.org). To quantify the CNAs of TRGs, they were represented as Genomic Identification of Significant Targets in Cancer (GISTIC) scores. Namely, an integer from -2 to $+2$ represents each of the five CNA types from deep deletion to amplification. A GISTIC score greater than 0 is considered amplified, less than 0 is considered deleted, and 0 represents the wild-type. Subsequently, we explored the differential expression of TRGs and prognostic differences in patients with and without CNAs.

2.5. Consensus clustering analysis of TRGs

To explore the heterogeneity of taurine metabolism in HCC, we used unsupervised clustering algorithms to cluster patients with HCC from the TCGA and ICGC cohorts into different molecular subtypes according to their differentially expressed TRGs. The "ConsensusClusterPlus" function from the "ConsensusClusterPlus" R package [26]was used after the expression data were scaled. Furthermore, to obtain the optimal number of clusters and increase the classification stability, the K-means clustering algorithm was performed with 1000 iterations and a resampling rate of 80%. In addition, other indicators, such as the consensus matrix, and consensus cumulative distribution function (CDF) were also considered. Next, the distribution difference of taurine metabolism subtypes was further distinguished using PCA and single sample gene set enrichment analysis (ssGSEA, using the "gsva" function in the "GSVA" R package) [27]. We then drew a heatmap (using "pheatmap" in the R package) and a stack bar chart to show expression patterns of TRGs across subtypes and the differences in patients' clinical parameters, including tumor grade, stage, patient age, sex, and survival status. The prognostic differences among subtypes were analyzed using Kaplan–Meier survival plots. The above steps were performed in the TCGA and ICGC cohorts.

2.6. Differential analysis between subtypes and enrichment analysis

DEGs among the two clusters were identified using the "limma" package in R, with the screening criteria set as |Log2FoldChange| > 1.5 and an adjusted p-value < 0.0001. Subsequently, we implemented Gene ontology (GO) annotation on the 78 DEGs through the WebGestalt database (http://www.webgestalt.org/)[28]. Then, GSEA was performed and visualized using the "ClusterProfiler" [29] and "GseaVis" R packages, respectively. Gene sets with a false discovery rate (FDR) < 0.25, p < 0.05, and normalized enrichment score (NES) > 1.5 were regarded as significantly enriched. To further characterize the differences in pathway activity of different taurine metabolic subtypes, we downloaded 50 predefined hallmark gene sets from the MSigDB database [30] and performed gene set variation analysis (GSVA) to calculate

the activity of each pathway using the "GSVA" R package; the results were presented in a heatmap. Additionally, we compared the activity of ten oncogenic pathways [31] using ssGSEA. To compare the cancer cell proliferation and metastasis abilities in different clusters, we downloaded 31 cell cycle progression-related genes and 200 epithelial mesenchymal transformation (EMT)-related genes from the literature [32] and the MSigDB database for ssGSEA analysis.

2.7. Comparison of CNVs between clusters

We downloaded copy number variation (CNV) data of the TCGA-LIHC cohort using the "TCGAbiolinks" R package and then performed online analysis using the GISTIC 2.0 module on the GenePattern website (https://cloud.genepattern.org/) to obtain GISTIC scores, which were visualized using ggplot2.

2.8. Immune cell infiltration analysis

Using the "IOBR" package [33], we quantified the abundance of 10 immune cell types in the TME for each HCC sample with expression data using the Microenvironment cell populations counter (MCP-counter) algorithm [34]. Besides, we calculated the immune score, ESTIMATE score, stromal score, and tumor purity using the ESTIMATE algorithm [35]. To further confirm that different clusters presented distinct immune landscapes, we divided the samples into four types of pan-cancer immune subtypes based on previous research [36]. Furthermore, we compared the gene expression of immune checkpoints (ICPs), major histocompatibility complex (MHC), immunosuppressive molecules, immunostimulatory molecules, chemokines, and chemokine receptors among the different subtypes.

2.9. Construction and validation of the risk signature

To construct a risk model for the clinical prediction of patients with HCC, we first performed univariate Cox regression analysis on 13 differentially expressed TRGs, 7 of which were survival-related DEGs (p < 0.05). To obtain the optimal prognostic biomarkers, we then implemented the LASSO regression analysis with the "glmnet" package to search for key genes associated with prognosis [37]. Five hub genes related to taurine metabolism were finally screened for model construction, which were *SLC36A1* (encoding solute carrier family 36 member 1), *GAD1* (encoding glutamate decarboxylase 1), *LRRC8D* (encoding leucine rich repeat containing 8 VRAC subunit D), *BAAT* (encoding bile acid-CoA:amino acid n-acyltransferase), and *CSAD* (encoding cysteine sulfinic acid decarboxylase). The predictive risk score was calculated as follows:

$$riskscore = \sum_{i=1}^{5} Coef(hubgene_i) * Exp(hubgene_i)$$

where Exp(gene) denotes the expression value of the gene and Coef (gene) represents the corresponding LASSO regularization coefficient. Subsequently, we conducted a risk score for each sample and divided the samples into high- and low-risk groups based on the median value. The distribution between the two subgroups was analyzed using PCA and t-distributed stochastic neighbor embedding (t-SNE).

Next, we investigated the relationship between the taurine-related prognostic signature (TRPS) and the clinicopathological parameters of patients with HCC, including sex, age, tumor grade, and stage. Kaplan–Meier analysis was used to compare overall survival (OS), disease specific survival (DSS), and progression free interval (PFI) between the TRPS subgroups. An alluvial diagram was applied to illustrate the distribution between different taurine metabolic subtypes and TRPS subgroups. In addition, the time-dependent receiver operating characteristic (ROC) and the area under the curve (AUC) values were applied to assess the accuracy of TRPS using the "pROC" package [38]. During the

construction of the TRPS, the TCGA-LIHC cohort was used as the training set, and the ICGC cohort and the combined GEO14250 and GEO76247 cohorts served as the validation sets. To assist researchers and clinicians in more easily predicting patient survival probability, we developed an online nomogram webserver for OS prediction using clinical parameters and a TRPS-based risk score in the TCGA cohort, it can be accessed at https://luqingsong.shinyapps.io/DynNomapp/.

2.10. TME landscape and immunotherapy response analysis

The MCP-counter algorithm was used to resolve the proportions of various immune cells in the different TRPS subgroups. To predict the response of samples to ICB therapies, we downloaded the immunophenoscore (IPS) data of the TCGA-LIHC cohort from The Cancer Immunome Atlas (TCIA) database (https://tcia.at/home), which is a superior predictor of response to anti-cytotoxic T lymphocyte antigen-4 (CTLA-4) and anti-PD-1 antibodies [39]. Tumor mutational burden (TMB) is also an important predictor of the efficacy of immunotherapy [40]; therefore, we used the "maftools" package to calculate the TMB of the samples and used KM-plots to show the OS of patients with high and low TMB and the predictive effect of TMB combined with the TRPS on patient OS.

Tumor immune dysfunction and exclusion (TIDE) is a novel and more accurate method to predict the outcome of patients treated with anti-PD1 or anti-CTLA antibodies [41]. Using the TIDE online tool (http://tide.dfci.harvard.edu), we calculated the TIDE score for each sample using the expression data from the TCGA and ICGC cohorts. Four immunotherapy cohorts providing detailed expression, survival, and immunotherapy efficacy data were used to validate the predictive ability of the TRPS for immunotherapy efficacy. Except for the IMvigor210 cohort, which was downloaded using the "IMvigor210CoreBiologies" R package, the rest of the cohorts were downloaded from the TIGER database, which integrates expression data with clinical outcomes from multiple immunotherapy cohorts.

2.11. Drug susceptibility and chemotherapy response analysis

Prediction of drug susceptibility was achieved using the "pRRophetic" package [42], which used the gene expression and drug sensitivity data in the Cancer Genome Project (CGP) as the training set to predict the sensitivity of multiple drugs using ridge regression [43]. Next, we validated the predictive power of TRPS on the response to chemotherapy using multiple cohorts, including the TCGA-cell carcinoma and endocervical adenocarcinoma (CESC) cohort, GSE20194, GSE50948, and GSE109211. In addition, the GSE50948 cohort was used to evaluate the potential of TRPS to predict the benefit of patients treated with transcatheter arterial chemoembolization (TACE).

2.12. Single-cell RNA-sequencing (scRNA-seq) analysis

The HCC scRNA-seq dataset was derived from GEO166635, which contained a total of 25,189 cells from two patients with primary liver cancer. The single-cell expression matrix was converted to a Seurat object using the Seurat R package (V 4.2.1) [44]. Quality control was then carried out and low-quality cells (< 300 and > 4000 genes/cell, < 3 cells/gene, and $> 15\%$ mitochondrial genes) were filtered out. Then, we selected the top 2000 highly variable genes using the "FindVariableFeatures" function and normalized the data using the "ScaleData" function. Subsequently, dimension reduction was performed using the "RunPCA" and "RunTSNE" functions, and clustering was implemented by the "FindNeighbors" and "FindClusters" functions (resolution = 0.5). Eventually, the 13,724 cells were divided into 15 cell clusters and annotated into corresponding cell types according to the canonical cell markers from previous articles and the "Cell annotation" tool in the CellMarker 2.0 database (http://117.50.127.228/CellMarker/)[45].

The "DimPlot" function was used to visualize cell types and a heatmap was drawn to show the expression of the corresponding markers in different cell types. A bubble plot drawn by the "DotPlot" function was used to show the expression patterns of TRGs in each cell type. Next, the "enrichIt" function in the "escape" R package was used to calculate the gene set enrichment scores for the scRNA-seq data, which was used to represent the taurine metabolic activity in single cells. Based on the median value of the ssGSEA score of all cells, we divided all cells into two groups and compared their cell-cell communication using the "CellChat" package [46].

To explore the heterogeneity of taurine metabolism among tumor cells at the single-cell level, a total of 499 epithelial cells were extracted for dimensionality reduction, clustering, and division into two clusters according to the markers found by the "FindAllMarkers" function. The stability of the clustering was verified by performing an NMF of the expression matrix of the epithelial cell subpopulations. Single-cell CNV analysis and CNV score calculation of each cell were performed using the "InferCNV" package [47]. The "monocle3" package was used to explore the relationship between cell pseudo-time trajectories and the expression patterns of TRGs [48].

2.13. Statistical analysis

Statistical analysis was performed using the R software (V 4.2.2). The Wilcoxon rank-sum test was used to evaluate the significance of the difference between two groups, and the Kruskal–Wallis test was used for comparisons between multiple groups. A log-rank test was used to define the differences between Kaplan–Meier survival curves. P-values < 0.05 were considered significant (* $P < 0.05$; ** $P < 0.01$; *** $P < 0.001$; **** $P < 0.0001$; ns: not significant).

3. Results

3.1. Genetic variation landscape of TRGs in HCC

We collected 17 TRGs from two pathways from the MSigDB database. PCA was used to distinguish 374 HCC tissues from 160 normal tissues based on TRG expression. The results showed that we could separate tumor tissues from normal tissues according to the expression levels of these genes (Fig. 1**A**), suggesting that HCC tissues have quite different taurine metabolic patterns from normal tissues and that taurine metabolism might play a role in the development of HCC. We then investigated the mRNA expression profiles of the 17 TRGs between tumor and normal tissues and identified 13 DEGs, among which 4 were upregulated and 9 were downregulated in tumor tissues (Fig. 1**B**). We then explored the genetic alteration profiles of these 13 differentially expressed TRGs in 371 patients with HCC in the TCGA-LIHC cohort. Among the 371 samples, the mutation frequency of TRGs reached 6.47%, and the mutation frequency of the top seven genes (*GAD1, SLC36A13, GAD2, GGT1, GGT5, CSAD*, and *LRRC8D*) with the highest mutation frequency were about 1%. Missense_Mutation was the main mutation type, while Splice_Site, Frame_Shift_Ins, Multi_Hit, and Frame_Shift_Del accounted for only a small fraction (Fig. 1**C and** Supplemental Figure. S1A). Genomic alteration data from the cbioportal database suggested that mutation was the predominant type of alteration in TRGs (Fig. 1**D**). We then explored the CNAs of the TRGs in detail. The results showed that each TRG had two types of CNA, amplification and deletion, but in different proportions. The majority of TRGs exhibited predominant CNAs of deletion, while amplification was observed as the predominant CNAs in a minority (Fig. 1**E**). Subsequently, we explored the relationship between the genomic alteration of TRGs and the prognosis of patients with HCC. Kaplan–Meier survival curves showed that patients without CNAs had significantly longer OS, PFI, and DSS than those with CNAs. However, there was no statistically significant difference in the disease-free interval (DFI) between patients with and without CNAs (Fig. 1**F-G,** Supplemental Figure. S1B), in addition, whether TRGs were mutated or not did not affect survival

Fig. 1. Differential analysis and genomic alteration analysis of taurine metabolism-related genes (TRGs) in TCGA-LIHC. (A) Principal component analysis for 17 TRGs displayed distinct gene expression patterns between tumor and normal samples. (B) Differential mRNA expression of TRGs between tumor and normal samples. (C) Mutation profiles of the 13 differentially expressed TRGs in 371 patients with HCC. (D) Genomic alteration profiles of the 13 differentially expressed TRGs in 353 patients with HCC. (E) Copy number variations of the 13 differentially expressed TRGs. (F and G) Kaplan-Meier curves of overall survival (OS) and progression free interval (PFI) between patients with and without copy number alterations of TRGs.

(Supplemental Figure. S1D). In terms of total genomic alteration, including mutations and CNAs, the unaltered group had a longer OS and DFS than the altered group, but the difference was not significant (Supplemental Figure. S1C). CNA of a gene can change its expression level. Therefore, we explored the expression levels of TRGs among groups with different CNA types. The results showed that amplification could significantly increase gene expression. while deletion decreased gene expression in most TRGs (Supplemental Figure. S1E).

3.2. Identification and validation of the taurine metabolic subtypes in HCC

To further explore the different expression patterns of TRGs in HCC, 371 HCC samples from the TCGA-LIHC cohort were used as a discovery cohort and 243 samples from the ICGC cohort were used as the validation cohort. We classified the samples into k groups (k = 2–4) based on the 13 differentially expressed TRGs using an unsupervised clustering algorithm via the "ConsensusClusterPlus" R package. Then, according to the minimum crossover in the consensus matrix and the smooth trend of the CDF curves, the optimal cluster number was determined to be two (Fig. 2A and Supplemental Figure. S2A-B). PCA of the 13 differentially expressed TRGs showed significant separation between the two clusters (Fig. 2B and Supplemental Figure. S2C). ssGSEA for the two pathways containing all the TRGs also revealed that all samples could be roughly divided into two subsets (Fig. 2C and Supplemental Figure. S2F), which further confirmed the stability of clustering. Subsequently, we compared the expression profiles of TRGs, clinical features, and prognostic differences of patients across the two clusters. The heatmap illustrated that all TRGs were differentially expressed between the clusters. The majority of the TRGs (9 out of 13) were upregulated in cluster 2, whereas four were downregulated (Fig. 2D and Supplemental Figure. S2D). In addition, there were significant differences in multiple clinical features between the two clusters, including age, sex, tumor stage, and grade. Specifically, Cluster 1 had a higher proportion of patients with histological grade 1–2 and tumor-node-metastasis (TNM) Stage I, while more patients with histological grade 3–4 and TNM Stage II–III belonged to cluster 2 (Fig. 2G). Furthermore, there were significant differences in OS and PFI between the two clusters: patients in cluster 1 had significantly longer OS and PFI than those in cluster 2 (Fig. 2E-F and Supplemental Figure. S2E). These results indicated that there was strong heterogeneity in taurine metabolism among patients with HCC and suggested that TRGs might play a role in the development and progression of HCC.

Differential analysis and functional enrichment analysis were subsequently performed to further evaluate the heterogeneity between the two clusters. Seventy-eight DEGs were screened out according to a threshold of |log2 fold change (FC)| > 1.5 and the adjusted p-value < 0.0001. A volcano plot was drawn to show the distribution of these DEGs (Supplemental Figure. S3A). GO annotation analysis of these DEGs indicated that they were potentially involved in metabolic processes and biological regulation (Supplemental Figure. S3B). GSEA analysis revealed that multiple cancer-related and immune-related pathways were significantly activated in cluster 2, such as the hippo signaling pathway and Fc gamma R-mediated phagocytosis, while many metabolism-related pathways, such as fatty acid degradation and amino acid metabolism, were significantly repressed (Supplemental Figure. S3C). Interestingly, some pathways that have been shown to be closely related to taurine metabolism were also enriched, such as primary bile acid biosynthesis and retinol metabolism (Supplemental Figure. S3D), the former of which is essential for digestion and the latter for vision. These results might imply that the physiological metabolic process of taurine was disrupted in HCC, and this disruption was associated with various carcinogenic processes.

3.3. Genomic features and the immune landscape of taurine metabolic subtypes

GSVA was performed to further evaluate the functional characteristics of the two clusters, and the GSVA enrichment score heatmap demonstrated that the two clusters had distinct pathway enrichment patterns (Fig. 3A-B). Most of the pathways composed of hallmark gene sets were significantly enriched in cluster 1, especially the metabolic pathway, which was consistent with the GSEA results in Section 3.2. We next compared the genomic features and plotted the mutation and copy number profiles of the two clusters. Overall, the GISTIC score distribution of the two clusters was similar (Fig. 3C). However, there were some cytobands in which the difference in CNV profiles was quite obvious, such as 1q42.2, 8q24.3, 13q32.3, and 13q34. Although none of the TRGs were located on the cytobands with the most significant CNV differences, 11 out of the 13 differentially expressed TRGs (not *GAD1* and *BAAT*) still had significant CNV differences between the two clusters (Supplemental Figure. S4A). Interestingly, the high expression of most genes (9 out of 13) in cluster 2 could be partially explained by their CNVs. According to their CNVs, the upregulated genes in cluster 2 showed more amplification or less deletion compared with the downregulated genes (Supplemental Figure. S4A-B). Furthermore, the total frequency of mutation was close between the two clusters (86.87% versus 87.5%); however, the most common mutated genes and their mutation frequencies in cluster 1 and cluster 2 differed significantly, with the top three most prevalent mutations in the former being *CTNNB1* (37%), *TP53* (27%), and *TTN* (27%), respectively, and in the latter being *TP53* (49%), *TTN* (27%), and *MUC16* (20%) (Fig. 3D). Considering that genomic alterations can stimulate cell-autonomous metabolic reprogramming and thus affect cell phenotypes [49,50], this might explain the predominant enrichment of metabolic pathways in cluster 1. Next, we compared the mutation profiles and activity differences of the 10 major oncogenic pathways between the two clusters (Fig. 3E-F). The results showed that the 10 pathways in cluster 2 were less affected by mutations compared with those in cluster 1. In addition, cluster 1 exhibited the highest proportion of samples affected by the WNT pathway (143/259), while cluster 2 demonstrated the highest proportion of samples affected by the TP53 pathway (48/96). Furthermore, except for the NRF2 pathway and the WNT pathway, whose activity was not significantly different from that of cluster 1, the activity of the other eight pathways in cluster 2 was significantly higher than that in cluster 1. Moreover, two factors, the cell cycle progression (CCP) score and the EMT score, which determine tumor proliferation and metastasis, respectively, were also calculated and compared between the two clusters. Both indicators were significantly higher in cluster 2 (Fig. 3G). These results suggested that cluster 2 might have a higher oncogenic activity, tumor proliferation, and metastasis ability than cluster 1, and might be associated with poor prognosis. Interestingly, these results were consistent with the molecular classification of HCC reported in several studies over the past decade. In cluster 1, it was CTNNB1 that presented the highest mutation frequency and WNT pathway presented the highest fraction of samples which was affected, while in cluster 2, the mutation frequency of TP53 was the highest and the TP53 pathway had the highest fraction of samples affected. This suggested that tumors in cluster 2 were more likely to belong to the "proliferation class" and therefore exhibited more aggression and led to a poorer prognosis, whereas tumors in cluster 1 were more likely to be classified as the "non-proliferation class", tending to toward maintenance of hepatocytic markers and a less aggressive phenotype [51–53].

The immune microenvironment can greatly affect the prognosis of patients and it is also closely related to tumor metabolism; therefore, we performed immune infiltration analysis using the MCP-counter algorithm for the two subtypes. As shown in the heatmap and boxplot (Fig. 4A-B), the two clusters presented distinct TMEs, and the abundance of 10 cell types in the TME was higher in cluster 2 than in cluster 1. In addition, cluster 2 demonstrated a higher Stromal score, Immune score,
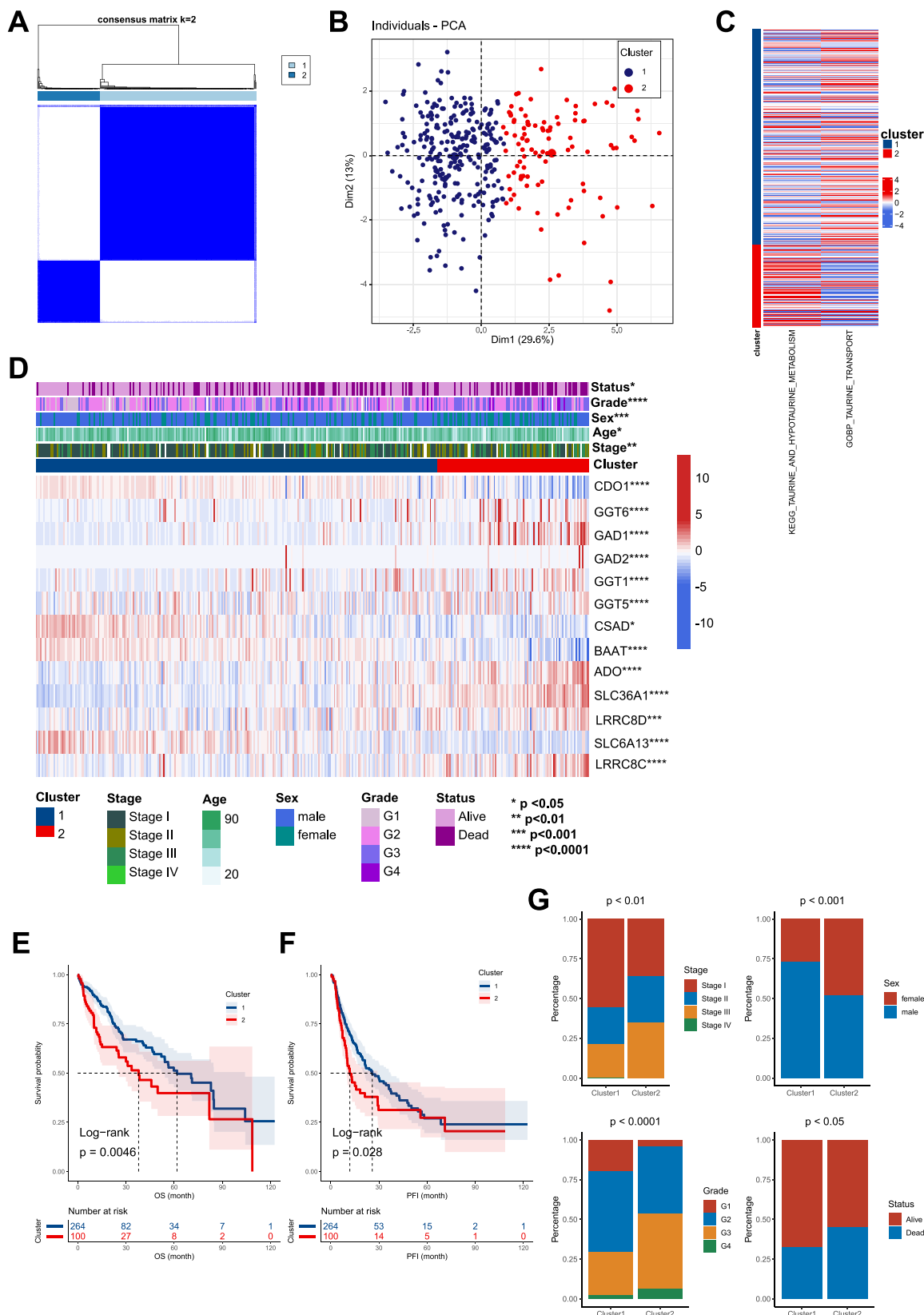
Fig. 2. Distinct taurine metabolism-related subtypes in the TCGA cohort. (A) Consensus clustering of the 13 differentially expressed TRGs and optimal classification for k = 2. (B) Principal component analysis based on the expression of 13 TRGs in the two subtypes. (C) Heatmap displaying single-sample gene set enrichment analysis (ssGSEA) scores of the two taurine-related pathways. (D) The expression heatmap of 13 TRGs in two clusters. Tumor stage, age, gender, stage, grade, and status were used as patient annotations. (E and F) Kaplan-Meier curves of OS and PFI between patients in the two subtypes. (G) Composition percentage of clinical features (survival status, gender, tumor grade, and stage) in the two subtypes.
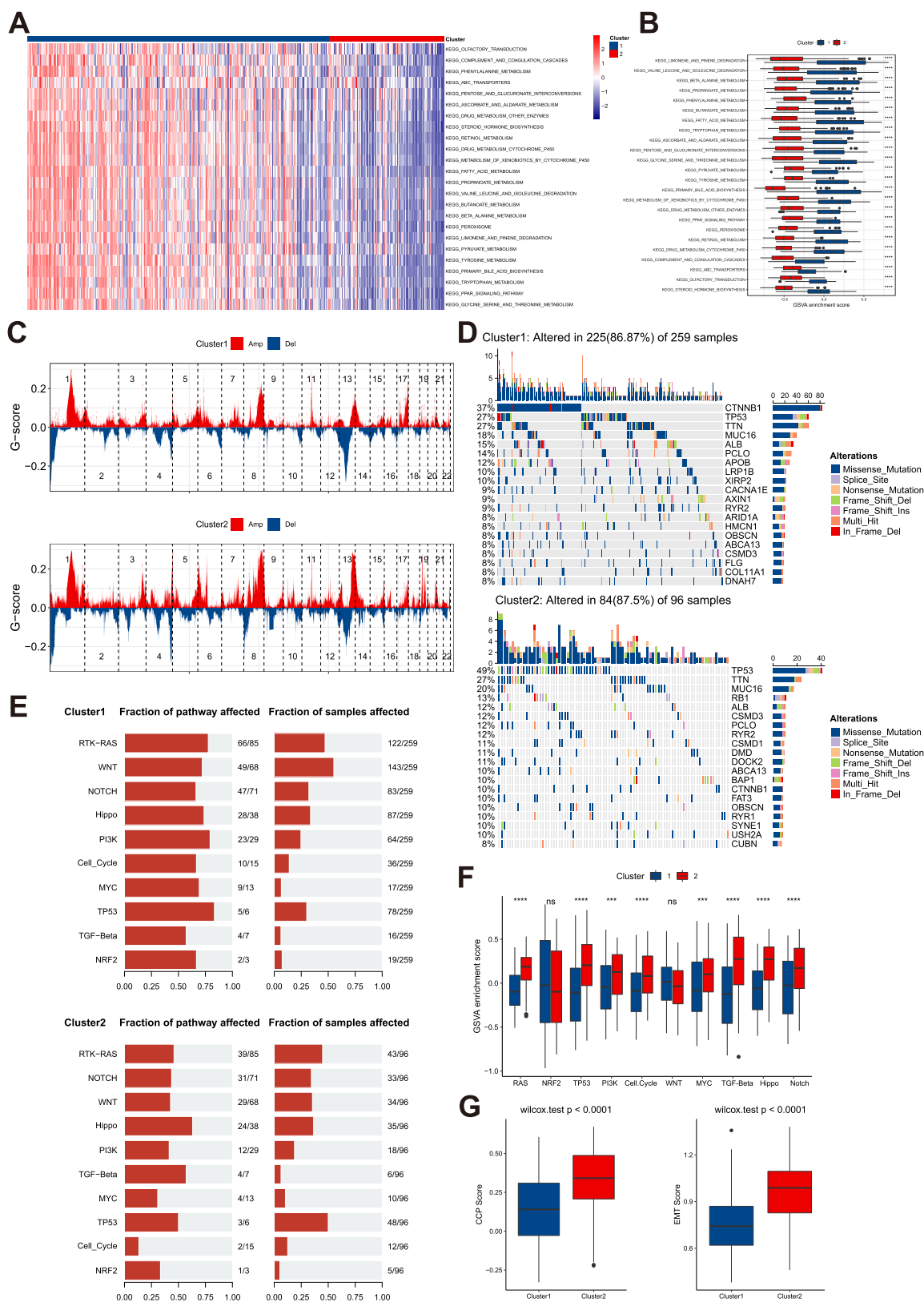
Fig. 3. Different genomic characteristics and oncogenic pathway activity of the two subtypes. (A and B) Heatmap and boxplot of GSVA enrichment scores based on the KEGG pathways in the two subtypes. (C) Comparison of copy number variations profiles between the two subtypes. (D) Comparison of mutation landscapes between the two subtypes. (E) Comparison of the ten oncogenic pathways affected by mutations between the two subtypes. (F) Boxplot of the GSVA enrichment scores of the ten oncogenic pathways in the two subtypes. (G) Boxplots of the CCP and EMT score in the two subtypes. GSVA: gene set variation analysis; KEGG: Kyoto Encyclopedia of Genes and Genomes; CCP: cell cycle progression; EMT: epithelial-mesenchymal transformation.
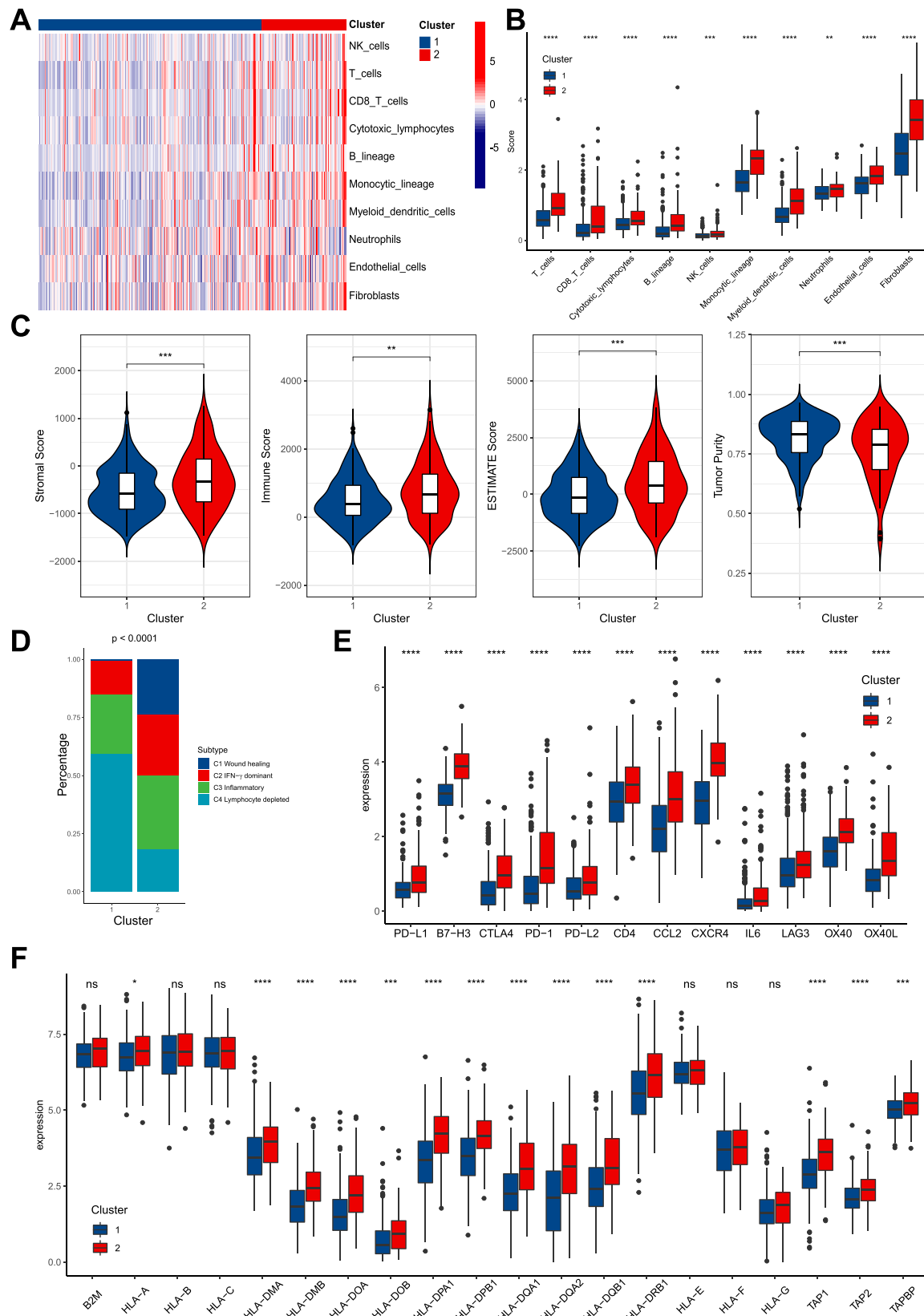
Fig. 4. Different immune landscapes between the two subtypes. (A and B) Heatmap and boxplot of the immune cell infiltration levels between the two subtypes. (C) Violin plots of the stromal score, immune score, ESTIMATE score, and tumor purity between the two subtypes. (D) Proportion of pan-cancer immunological subtypes in the two subtypes. (E and F) Boxplots of gene expression of immune checkpoints and MHC gene sets between the two subtypes.

and Estimate score, but a lower tumor purity score, compared with cluster 1(Fig. 4C). Consistent with the results of the MCP-counter algorithm, this also implied that cluster 2 had a higher abundance of immune cells and immune molecules. To further explore the immunophenotypes of these clusters, we compared the proportion of immune subtypes between the two clusters based on pan-cancer immune subtypes reported by Thorsson, et al. [36]. Patients with HCC in cluster 1 showed a high proportion of lymphocyte-depleted subtypes and a very low proportion of wound healing subtypes. In contrast, cluster 2 showed a more balanced proportion of various immune subtypes (Fig. 4D). Next, we evaluated the expression of multiple immune molecules between the two clusters, including major histocompatibility complexes, immune checkpoints, co-stimulators and co-inhibitors, chemokines, and their receptors, which represented important aspects of anti-tumor immunity, such as antigen presentation, tumor killing, and immune escape (Fig. 4E-F and Supplemental Figure. S5A-D). Compared with those in cluster 1, cluster 2 displayed the significantly higher expression of a series of immune molecules, except MHC class I molecules. This might indicate distinct immune escape mechanisms between these two subtypes, namely defective antigen presentation capacity and overexpression of immunosuppressive molecules. Taken together, these results illustrated a very different immune landscape between the two subtypes and implied that different therapeutic measures might be required for the different subtypes.

3.4. Construction and validation of a prognostic risk model

To construct a risk model to evaluate clinical prognosis and treatment choice in patients with HCC, we first performed univariate Cox regression analysis on the 13 differentially expressed TRGs in the TCGA-LIHC cohort, thereby identifying 7 survival-related DEGs (Fig. 5A). Then, using LASSO regression analysis, according to the minimum partial likelihood deviance value and the maximum concordance index (C-index), we determined the optimal lambda and thus obtained five prognosis-related hub genes and their respective LASSO regularization coefficients (Fig. 5B-E). Eventually, the optimal risk model, TRPS, was constructed according to the weighted sum of gene expression: risk score $= SLC36A1 \times (0.197) + GAD1 \times (0.148) + LRRC8D \times (0.130) + BAAT \times (-0.108) + CSAD \times (-0.194)$. All patients with HCC evaluated by the TRPS were split into high-risk and low-risk subgroups based on the median value in the TCGA cohort. The risk score plot showed that patients suffered poorer survival status and survived for a shorter time in the high-risk group compared with those in the low-risk group (Fig. 5F). In addition, the heatmap showed that the five hub genes had significantly different expression patterns in the two subgroups, in which *LRRC8D*, *SLC36A1*, and *GAD1* were upregulated in the high-risk group, while *BAAT* and *CSAD* were upregulated in the low-risk group (Fig. 5G). The PCA and t-SNE algorithms demonstrated different distribution patterns between the two groups of HCC patients (Fig. 5H-I).

We then focused on the potential of the TRPS as an indicator of prognosis in patients with HCC. Firstly, the relationship between the expression levels of five hub genes used for model construction and the prognosis of patients with HCC was explored. Kaplan–Meier plots identified two protective genes (*BAAT* and *CSAD*) and three risk genes (*SLC36A1*, *GAD1*, and *LRRC8D*) (Supplemental Figure. S6A-E). Next, survival analysis revealed that the high-risk group had significantly shorter OS ($p < 0.0001$), DSS ($p < 0.0001$), and PFI ($p < 0.05$) compared with the low-risk group (Fig. 5J-L). Importantly, combining univariate and multivariate regression analyses, the TRPS was identified as an independent prognostic factor in patients with HCC (Fig. 6A-B). In addition, the TRPS could be used to stratify the clinical features of HCC patients: those patients older than 60 years of age, male, and with lower tumor grade and stage, generally exhibited a lower risk score, whereas patients younger than 60 years of age, female, and with higher tumor grade and stage, possessed a higher risk score (Fig. 6C-F). We also compared the risk scores between the two different metabolic subtypes

(Fig. 6G), and the results showed that cluster 2 presented a significantly higher risk score than cluster 1, which might also be associated with the poor prognosis of patients in cluster 2. An alluvial plot and a table displayed the summary results of the distribution of multiple clinical features in the patients (Fig. 6H and Supplemental Table. S1). The predictive performance of the risk score was subsequently assessed using a ROC curve, yielding AUC values of 0.738, 0.668, and 0.637 for 1-, 3-, and 5-year survival predictions, respectively (Fig. 6I). Finally, two independent external cohorts, the ICGC cohort and the integrated GSE14520 and GSE76427 cohorts, were introduced to assess the generalization capability of the TRPS. We performed the same analysis for these two cohorts as in the TCGA-LIHC cohort, and the TRPS demonstrated its ability to stratify and assess the prognosis of both cohorts (Supplemental Figure. S7A-H).

3.5. Evaluation of the TME and prediction of immunotherapeutic responses

To assess the TME in different risk subgroups, we quantified 10 cell types in the TME of patients in the high- and low-risk groups. The heatmap demonstrated the distinct TMEs between the two groups and further quantification showed that except for neutrophils and endothelial cells, the abundance of the remaining eight cell types in the high-risk group was significantly higher than that in the low-risk group (Fig. 7A-B). Correlation analysis showed that monocytic lineage cells had the highest correlation with the risk score, followed by T cells and myeloid dendritic cells, while neutrophils and endothelial cells had the lowest correlation (Fig. 7C). This might hint at the cell groups most affected by taurine metabolism in the immune microenvironment. In addition, a variety of immune-related genes were also expressed at high levels in the high-risk group, including antigen-presenting molecules, immune checkpoint molecules, immunostimulatory and immunosuppressive molecules, chemokines, and their receptors (Fig. 7D-E). This not only suggests that the two groups of patients had distinct immunophenotypes: the low-risk group had characteristics of a TME closer to "cold" tumors, while the TME of the high-risk group was closer to that of "hot" tumors and might respond differently to immunotherapy, but also indicated that patients in the high-risk group might receive more clinical benefits from ICB therapy than those in the low-risk group. Next, we used the immunophenoscore to predict the response to anti-PD1/anti-CTLA4 therapy in the high- and low-risk groups. The results showed that among PD1-negative patients, patients in the low-risk group were more sensitive to immunotherapy, regardless of the expression level of CTLA-4, while PD1-positive patients showed no significant difference in immunotherapy response, regardless of CTLA4 level (Fig. 7F). Although there was no significant difference in TMB between the two groups (Fig. 7G), using both the TMB alone and in combination with the risk scores to predict outcomes of patients achieved satisfactory results. As expected, the survival analysis demonstrated that patients with a higher TMB and a higher risk score experienced poorer prognosis (Fig. 7H-I).

To further elucidate the relationship between TRPS and the efficacy of immunotherapy, we used a series of previously reported biomarkers to predict immunotherapy responses in the TCGA and ICGC cohorts, respectively, including the TIDE score, the microsatellite instability (MSI) score, the T cell exclusion score, the T cell inflamed score, myeloid-derived suppressor cells (MDSC)s, and the T cell dysfunction score. In the two cohorts, these markers were significantly different between the two groups. The TIDE score, the T cell exclusion score, the T cell inflamed score, and MDSC were significantly lower in the high-risk group than in the low-risk group, while the MSI and T cell dysfunction scores were significantly lower in the low-risk group (Fig. 8A-B). Since a higher TIDE score implied a higher likelihood of immune escape with a worse outcome, and a lower MSI was associated with fewer immunotherapy responses, these indicators imply that patients in the high-risk group were more likely to benefit from immunotherapy than those in the low-risk group. In addition, the proportion of patients responding to
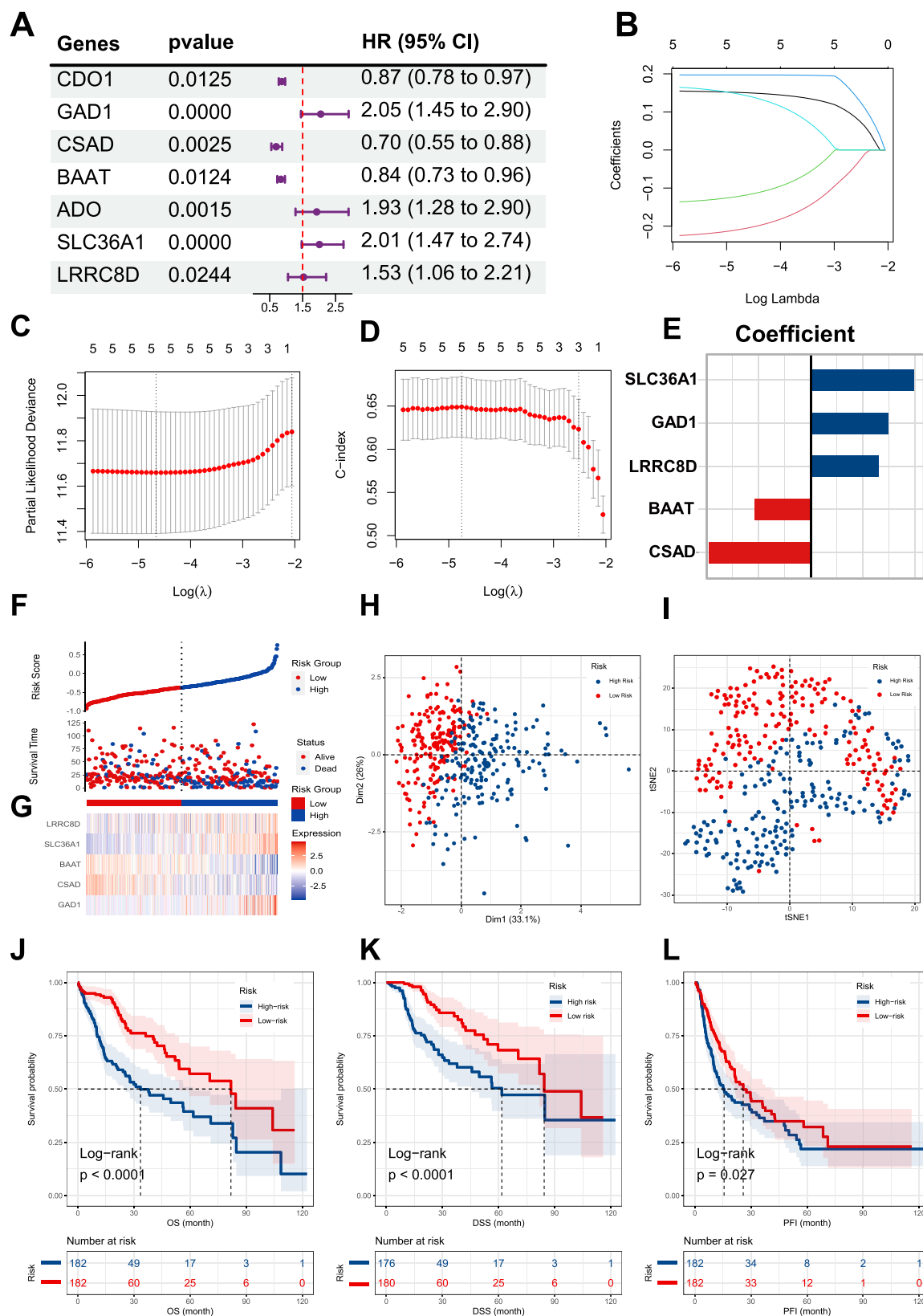
Fig. 5. Construction of the taurine-related prognostic signature (TRPS) in TCGA-LIHC cohort. (A) Univariate Cox regression analysis identified 7 survival-related genes from 13 differentially expressed TRGs. (B) LASSO coefficient profiles of the 7 survival-related genes. (C and D) Five hub genes were retained to construct the risk model according to the minimum partial likelihood deviance and maximal C-index. (E) LASSO regularization coefficients of the five hub genes. (F) Distribution plot of the risk score and survival status between the high-risk and low-risk groups. (G) Gene expression of the five hub genes used for model construction in the high-risk and low-risk groups. (H and I) PCA plot and t-distributed stochastic neighbor embedding (t-SNE) plot display the distribution of patients in the high - and low-risk groups. (J, K, L) Kaplan-Meier curves of OS, DSS, and PFI between patients in the high - and low-risk groups. OS: overall survival; DSS: disease-specific survival; PFI: progression-free interval.
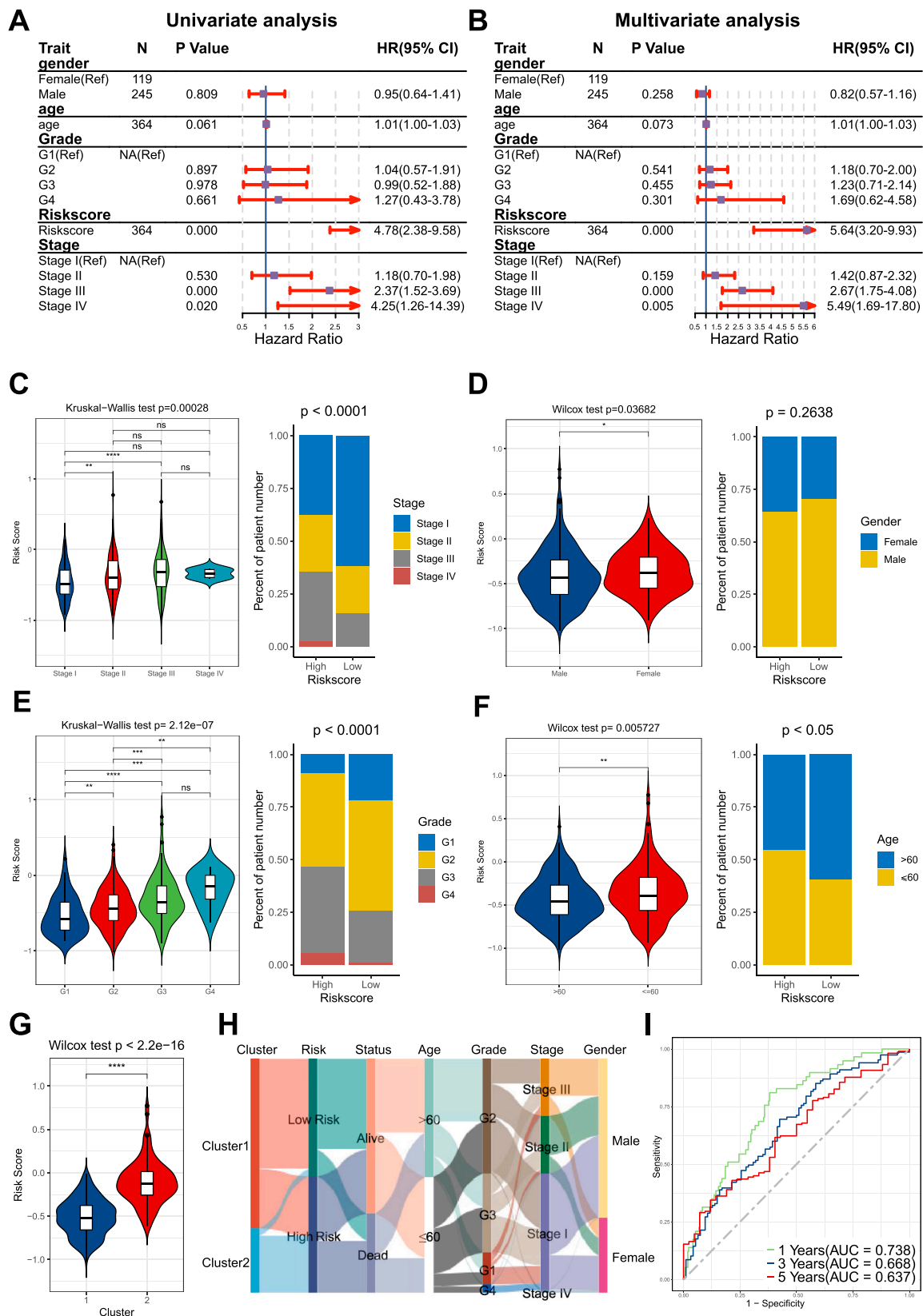
Fig. 6. Correlation between the risk score and clinical characteristics. (A and B) Forest plots of the univariate Cox and multivariate Cox analysis. (C, D, E, F) The difference in risk score by multiple clinical characteristics, such as age, gender, tumor grade, and stage (left), composition percentage of the two groups in these clinical characteristics (right). (G) Comparison of the risk score between the two subtypes. (H) Alluvial diagram displaying the distribution of patients. (I) Receiver operating characteristic curves of the risk model in predicting prognosis.
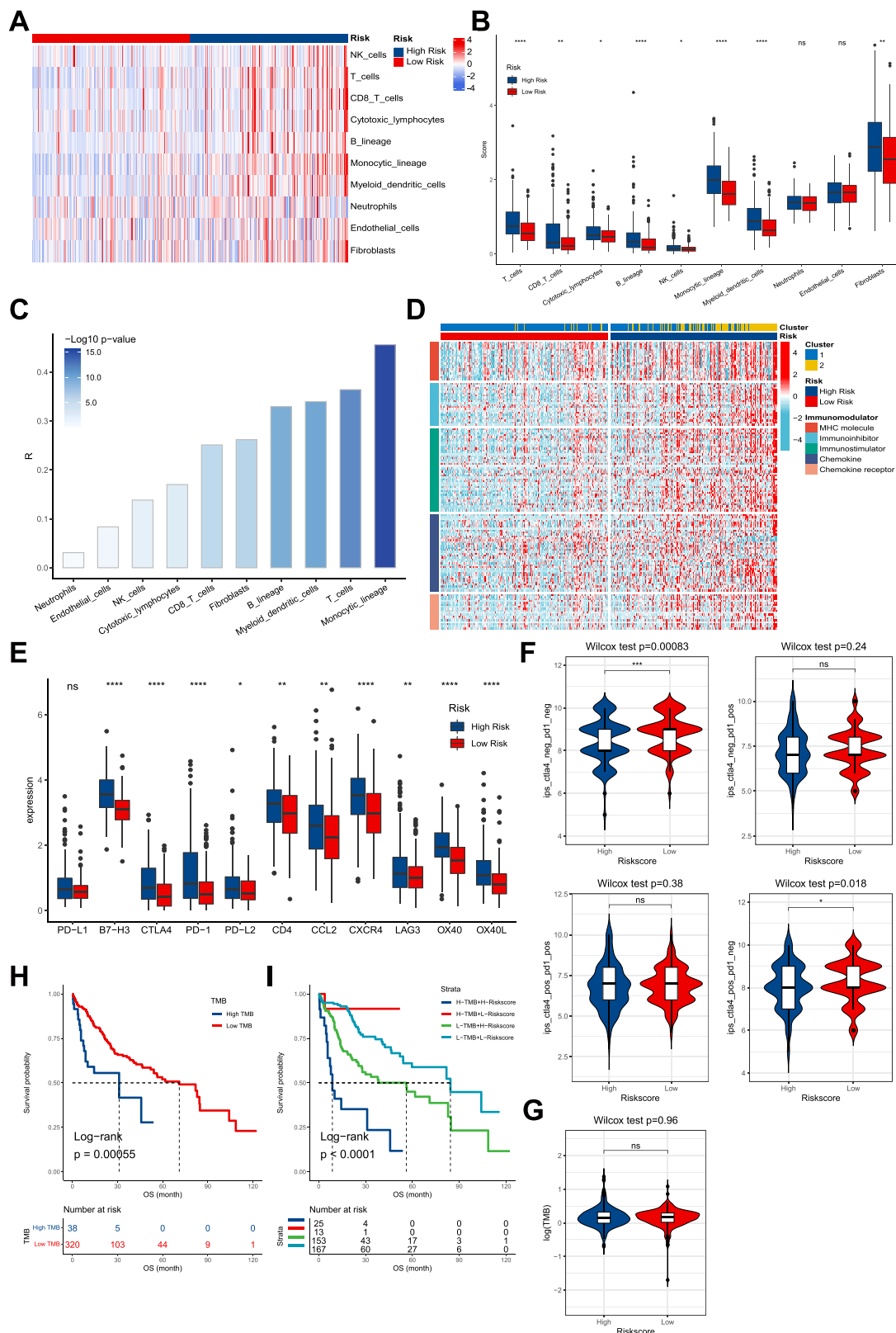
Fig. 7. Correlation of the risk score and immune cell infiltration in high- and low-risk groups. (A and B) Heatmap and boxplot of the immune cell infiltration levels in the high-risk and low-risk groups. (C) Spearman correlation coefficients between the risk score and immune cell infiltration. (D) Heatmap of gene expression of various immune-related molecules in high- and low-risk groups. (E) Boxplot of gene expression of immune checkpoints in the high-risk and low-risk groups. (F) Comparison of the immunophenoscore (IPS) between the high- and low-risk groups. (G) Comparison of TMB between the high- and low-risk groups. (H) Kaplan-Meier curves of OS between patients in the high - and low-TMB groups. (I) Kaplan-Meier curves of OS between patients stratified by both TMB and the risk score. TMB: tumor mutational burden.
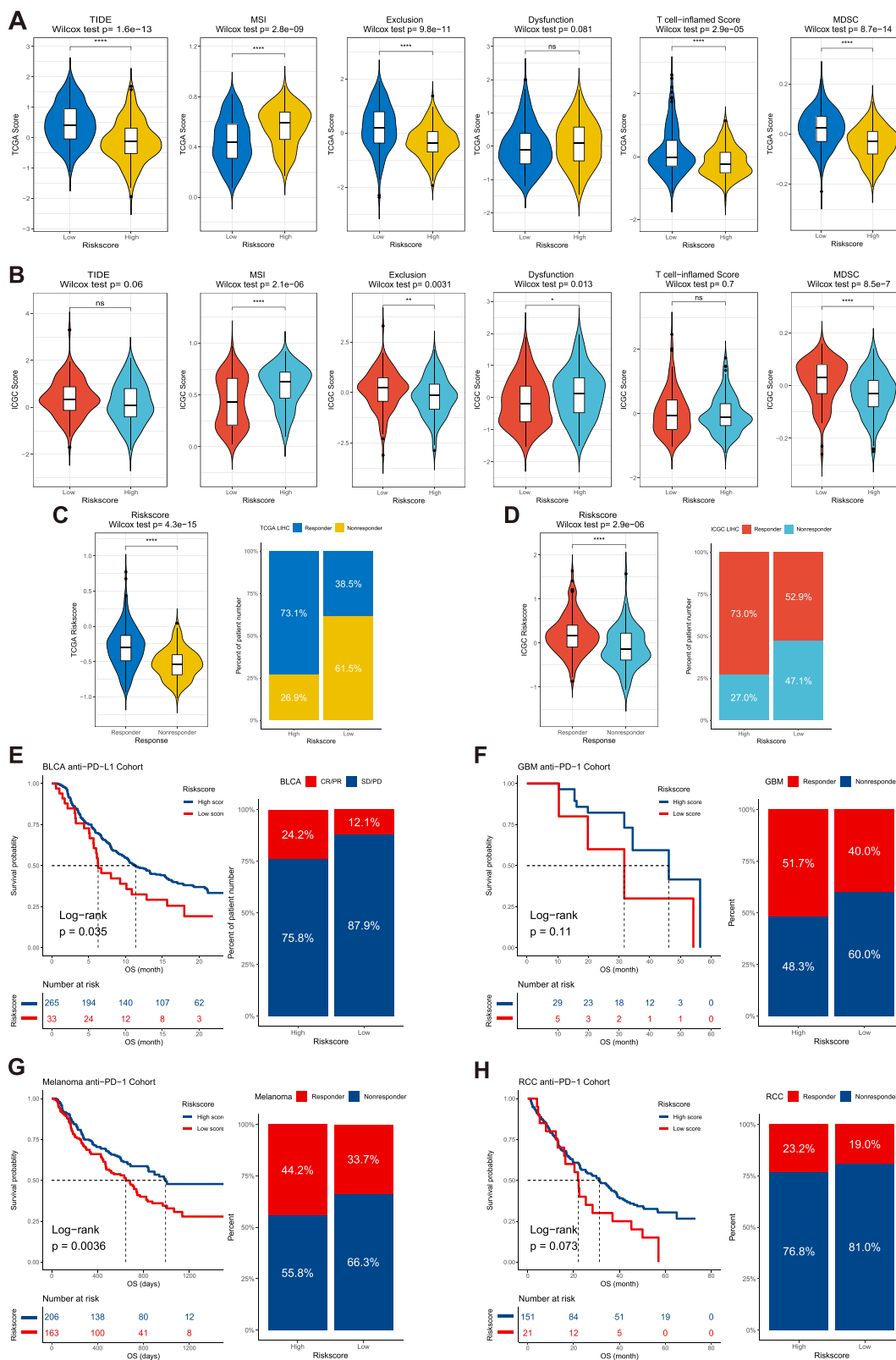
Fig. 8. Prediction and validation of immunotherapy response by the risk model. (A and B) Comparison of multiple predictors such as tumor immune dysfunction and exclusion (TIDE) score, microsatellite instability (MSI), Exclusion score, T cell-inflamed score, and myeloid-derived suppressor cell (MDSC) values between the high- and low-risk groups in TCGA and ICGC cohorts. (C and D) Comparison of the risk score between responders and non-responders predicted by the TIDE website (left). The percentage of patients with clinical response to immunotherapy in high- and low-risk groups (right). (E, F, G, H) Kaplan-Meier curves for patients with high versus low TRPS in multiple anti-PD1/anti-PD-L1 immunotherapy cohorts(left). The percentage of patients with clinical response (CR/PR: complete response / partial response; SD/PD: stable disease/ progressive disease to immunotherapy in high- and low-risk groups (right).

immunotherapy in the different risk groups was also assessed and as expected, the results were consistent, with responders having significantly higher risk scores than non-responders and a much higher proportion of responders in the high-risk group than in the low-risk group (Fig. 8C-F). Next, we validated the predictive performance of the TRPS on immunotherapy benefit in multiple independent external cohorts across multiple cancers treated with anti-PD1/PD-L1 antibodies, including bladder urothelial carcinoma (BLCA) (Fig. 8E), glioblastoma multiforme (GBM) (Fig. 8F), melanoma (Fig. 8G), and renal cell carcinoma (RCC) (Fig. 8H). Survival analysis showed that in the BLCA and melanoma immunotherapy cohorts, patients in the high-risk group presented significantly longer OS compared with those in the low-risk group (p = 0.035 for BLCA and p = 0.0036 for melanoma). Besides, in the GBM and RCC immunotherapy cohort, the high-risk group also showed a better survival benefit, although it was not significant (p = 0.11 for GBM and p = 0.073 for RCC). Furthermore, a higher percentage of patients in the high-risk group benefited from immunotherapy than in the low-risk group in all four cohorts, suggesting that patients in the high-risk group were more sensitive to immunotherapy. These results revealed that the TRPS might serve as a potential biomarker to evaluate the efficacy of immunotherapy in patients, and further suggested that taurine metabolism might play a potential role in anti-tumor immunity and thus influence the efficacy of immunotherapy.

3.6. Drug susceptibility analysis and the prediction of chemotherapeutic responses

Chemotherapy is one of the most important treatment strategies for advanced liver cancer. Therefore, we performed drug susceptibility analysis and calculated the IC50 values of ten common chemotherapy drugs for liver cancer using the ridge regression algorithm (Supplementary Table 2). By comparing the IC50s of these ten drugs between the two groups, we found that patients in the high-risk group were significantly more sensitive to all ten drugs than the low-risk group (p < 0.01 for Sorafenib, p < 0.0001 for Doxorubicin, p < 0.001 for Paclitaxel, p < 0.0001 for 5-Fluorouracil, p < 0.0001 for Gemcitabine, p < 0.0001 for Methotrexate, p < 0.01 for Bortezomib, p < 0.0001 for Rapamycin, and p < 0.001 for Vinblastine) (Fig. 9A-J). This suggested that patients in the high-risk group would receive more clinical benefit from chemotherapy. We then introduced several independent external cohorts to validate this hypothesis, including a CESC cohort from the TCGA database treated with cisplatin, a breast cancer cohort (GSE20194) treated with cyclophosphamide, doxorubicin, fluorouracil, and paclitaxel, a colorectal cancer cohort (GSE28702) treated with fluorouracil, leucovorin, and oxaliplatin, and a HCC cohort (GSE109211) treated with sorafenib. The results showed that these patients who responded to chemotherapy possessed a higher risk score compared with that of the low-risk group (p = 0.039 for TCGA-CESC cohort (Fig. 9K), p < 0.0001 for GSE20194 (Fig. 9L), p = 0.056 for GSE28702 (Fig. 9M), and p = 0.0063 for GSE109211 (Fig. 9N)). In addition, patients in the high-risk group displayed a higher proportion of responders than those in the low-risk group (Fig. 9P-S). Subsequently, ROC curves were used to evaluate the predictive performance of the TRPS for chemotherapy response, and the AUC values of TRPS were 0.746 (Fig. 9U), 0.693 (Fig. 9V), 0.622 (Fig. 9W), and 0.707 (Fig. 9X) in the four cohorts, respectively. Given that TACE is currently a commonly used chemotherapy method for liver cancer in clinical practice, we specifically investigated the predictive performance of the TRPS on the benefit to patients treated with TACE. We conducted the same analysis in the liver cancer cohort GSE50948 treated with TACE. Surprisingly, unlike previous results, the risk score of the responders was lower (p < 0.0001) and the proportion of responders was significantly higher in the low-risk group than in the high-risk group (Fig. 9O, T). In addition, the TRPS had an AUC value of 0.767 in this cohort (Fig. 9Y).

3.7. Analysis of taurine metabolism at single-cell resolution

To further determine the metabolic pattern of taurine in the TME of HCC at the single-cell level, the single-cell dataset GSE166635, containing a total of 25,189 cells from two primary HCC tissues, was collected and analyzed in depth. After rigorous quality control, 13,724 cells were retained for further analysis. We then performed the standard procedure using the "Seurat" package and carried out dimension reduction and clustering for the single-cell expression matrix. A resolution of 0.5 was selected and 15 cell clusters were obtained (Fig. 10A). Next, we preliminarily divided the cells into immune cells, epithelial cells, and stromal cells based on the expression of CD45 and EPCAM (Fig. 10B). Each cell was then annotated to the appropriate cell type based on the classical markers collected from previous literature and the "CellMarker" database (Fig. 10C). The heatmap displayed these 15 cell types and the expression of their corresponding markers (Fig. 10D). Next, a bubble plot was drawn to investigate the expression of all TRGs in various cell types within the TME (Fig. 10E), and the results showed that most TRGs presented distinct expression patterns in these 15 cell types. Notably, we found that some TRGs are specifically expressed in certain cells, such as *GGT1*, *BAAT*, and *SLC6A11* in epithelial cell; *GGT5* in fibroblasts; *SLC36A1* in tumor-associated macrophages (TAMs); *LRRC8A*, *SLC6A6*, and *LRRC8C* in endothelial cells. To explore the potential roles played by different cell types in taurine metabolism in more detail, we classified TRGs as metabolism-related and transport-related genes and calculated the metabolic activity and transport activity of each of the 15 cell clusters separately using the ssGSEA algorithm (Fig. 10F-G). The results revealed that in the TME of patients with HCC, epithelial cells showed the highest metabolic activity and immune cells showed the highest transport activity, while stromal cells presented the lowest taurine metabolism and transport activity. In addition, we divided all cells into a high- and a low-metabolic group according to their metabolic activity and discussed the differences in cell-cell communication between the two groups (Fig. 10H). There was little difference in the number of inferred interactions between the two groups; however, the strength of the interactions was significantly higher in the low-metabolic group than in the high-metabolic group (Fig. 10I-J). Furthermore, the interaction network diagrams revealed that CD8 +T cells were mainly responsible for the significant increase in cell communication strength in the low-metabolic group compared with that in the high-metabolic group (Fig. 10K-L). Moreover, by further comparison of ligand-receptor pairs of CD8 + T cells between the two groups, we found that all interactions between other cells and CD8 + T cells in the high metabolic group were reduced or lost to varying degrees compared with the cells in the low metabolic group, but mainly focused on a significant reduction in the interaction of MHC-I class molecules with CD8 subunits of CD8 + T cells (Fig. 10M). This implied a diminished antigen presentation capacity, as well as enhanced immune escape of tumor cells in the high metabolic activity group. Notably, we also observed an increase in the strength of the SPP1-CD44 and CCL5-ACKR1 axes in the low-metabolic group (Fig. 10M-N), and their activation has been shown to promote the polarization of macrophages to M2-like tumor-associated macrophages [54,55] and tumor angiogenesis [56] in the TME, respectively. These results suggested that taurine metabolism might play a role in a variety of biological processes in tumors and is involved in regulating the anti-tumor immune process in a very complex manner.

3.8. Heterogeneity of taurine metabolism in malignant cells

To further investigate the metabolic heterogeneity of taurine in malignant cells, the same analysis was performed on extracted epithelial cell subsets. Using the marker genes found by the "FindAllMarkers" function with a resolution of 0.05, we divided the epithelial cells into two subsets, denoted as C0 and C1 (Fig. 11A). The stacked violin plot showed the corresponding markers of these two groups of cells

(caption on next page)

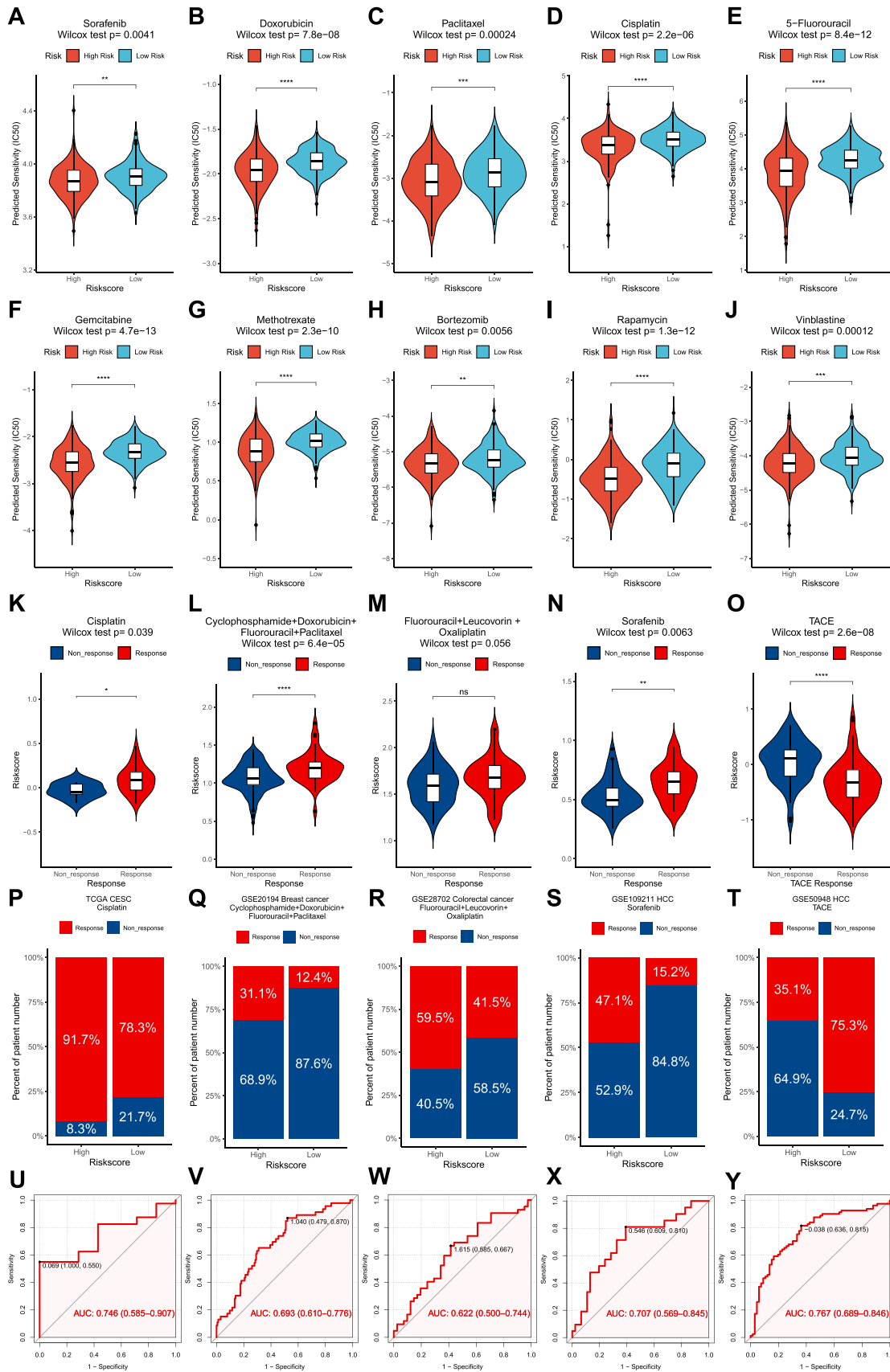**Fig. 9.** Prediction and validation of chemotherapeutic response by the risk model. (A–J) Comparison of the sensitivity for sorafenib (A), doxorubicin (B), paclitaxel (C), cisplatin (D), 5-fluorouracil (E), gemcitabine (F), methotrexate (G), bortezomib (H), rapamycin(I) and vinblastine (J) in patients at low and high risk. (K, L, M, N) Comparison of the risk score between responders and non-responders in multiple chemotherapy cohorts treated with different drugs. (P, Q, R, S) The percentage of patients with clinical response to chemotherapy in high- and low-risk groups for TCGA-CESC (P), GSE20194 (Q), GSE28702 (R), GSE109211(S). (U, V, W, X) Receiver operating characteristic curves and the area under the curve (AUC) values of the risk model in predicting chemotherapy response for TCGA-CESC (U), GSE20194 (V), GSE28702 (W), GSE109211 (X). (O) Comparison of the risk score between responders and non-responders in the HCC chemotherapy cohort treated with trans-catheter arterial chemoembolization (TACE). (T) The percentage of patients with clinical response to TACE in high- and low-risk groups. (Y) ROC curve and AUC value of the risk model in predicting clinical response for patients treated with TACE.

(Fig. 11B). Next, we used the NMF algorithm on the epithelial cell subpopulations based on the expression levels of TRGs and selected 2 as the best rank value according to the cophenetic, dispersion, and silhouette indicators, thus dividing the epithelial cells into two clusters, denoted as cluster 1 and cluster 2 (Fig. 11C and Supplemental Figure. S8A). Then, the t-SNE algorithm was used to show the distribution of these two clusters (Fig. 11D). The distributions of epithelial cells obtained using the two approaches were highly coincident, which further confirmed the different subtypes of taurine metabolism in epithelial cells and validated our results obtained by the consensus clustering algorithm in the bulk transcriptome. Subsequently, to identify malignant cells among epithelial cells, we used the "inferCNV" algorithm to find large copy number variants in somatic chromosomes in epithelial cells. In this process, a portion of endothelial cells and fibroblasts were used as reference controls, and the remaining endothelial cells and fibroblasts, as well as epithelial cells, were used as the input. The heatmap showed significant over-abundance or lower abundance of the genome in all epithelial cells compared with endothelial cells and fibroblasts in the control group, indicating that all epithelial cells were malignant (Supplemental Figure. S8B). We next quantified the CNV in each cell and compared the CNV score between C0 and C1, showing that the cells in the C1 subset presented higher CNV scores compared with those in C0 (Fig. 11E). The ssGSEA score heatmap of 50 hallmark pathways further demonstrated the heterogeneity of the two subsets in terms of malignant cells (Supplemental Figure. S8C). As before, we compared the taurine metabolic and transport scores of C0 and C1, respectively (Fig. 11F-G). The results showed that the cell transport activity in C1 was significantly higher than that in C0, while the metabolic activity in C1 was lower than that in C0. In addition, the heatmap demonstrated two subgroups with high metabolic and transport activity, respectively (Fig. 11H). We performed differential analysis for these two subgroups and subsequently selected the top ten genes with the highest fold change in each subgroup for GO enrichment analysis (Supplemental Figure. S8D). The results showed that most DEGs were highly expressed in the metabolic subsets, and only three genes were highly expressed in transport subsets, namely, *S100A6*, *S100A11*, and *LGALS3* (Supplemental Figure. S8E). GO analysis showed that genes in the metabolic subpopulation were mainly enriched in protein-lipid metabolic pathways, while genes in the transport subpopulation were significantly enriched in immune-related pathways such as T-cell activation, antigen presentation, and immunological synapse formation. Furthermore, GSEA analysis revealed that cells in metabolic subpopulations were closely related to many important pathways, such as complement and coagulation cascades, cholesterol metabolism, oxidative phosphorylation, and ferroptosis (Fig. 11I), which have been shown to play a potential role in the development and progression of HCC. Moreover, pseudo-time analysis illustrated the dynamic transcriptional state of TRGs in the trajectory process of epithelial cells. We selected the cells with the lowest malignancy (exhibiting the smallest CNV score) as the root of the trajectory, and in the figure, numbers with white circles indicated different outcomes and black circles indicated bifurcation points in terms of cell fates (Fig. 11J). The trajectory manifold showed that the epithelial cells developed from a transcriptional state dominated by taurine metabolism to a transcriptional state dominated by transport (Fig. 11K). At the same time, the expression of most TRGs was upregulated during this process (Fig. 11L), which might imply that tumor cells hijacked large amounts of taurine from the microenvironment as they progressed, just as they do with

methionine [57].

4. Discussion

HCC is the most prevalent histological subtype of primary liver cancer, and is highly heterogeneous, which greatly affects the prognosis of patients, resulting in high mortality and a five-year survival rate of less than 20% [2]. Over the past decade, the clinical practice of immunotherapy, especially ICB therapy, had achieved great success in the treatment of various cancers and completely revolutionized the treatment of liver cancer [58]. However, multiple clinical trials demonstrated that the ORR to anti-PD1/anti-PD-L1 antibodies in patients with HCC ranges from a disappointing 10–20% because of the presence of a suppressive immune microenvironment [59,60]. Therefore, identifying patients that can benefit from immunotherapy becomes urgent, which calls for the development of indicators that can more accurately predict the efficacy of immunotherapy to guide optimal clinical interventions. To the best of our knowledge, this was the first study to determine the molecular subtypes associated with taurine metabolism and to establish a risk model to predict prognosis, the efficacy of immunotherapy, and the chemotherapeutic response, as well as exploring the heterogeneity of taurine metabolism within the TME at the single-cell level.

In this study, we comprehensively investigated the metabolic heterogeneity and potential roles of taurine in HCC through multi-omics bioinformatics analyses, such as genomics, transcriptomics, and single-cell transcriptome profiling. Firstly, we discriminated HCC tissues from normal controls according to the expression profiles of TRGs. Then, we screened differentially expressed TRGs and explored their mutation and CNV profiles, as well as the relationship between these genomic alterations and patient prognosis. Next, we identified and validated two heterogeneous subtypes of taurine metabolism in HCC using a consensus clustering algorithm on the training and validation sets, respectively. After that, we constructed the TRPS using five hub genes screened by Cox regression and LASSO analysis and divided patients into high- and low-risk groups. Next, we compared the clinicopathological features of the two groups of patients and assessed the predictive performance of the model using ROC analysis in two independent external cohorts. The results showed that TRPS was not only an independent factor for the clinical prognosis of patients, but also achieved relatively high performance in short- and long-term survival prediction (1-year OS, AUC = 0.738 in the TCGA cohort, 4-year OS, AUC = 0.802 in the ICGC cohort). In addition, we analyzed the TME of the two groups and predicted the effect of immunotherapy using multiple indicators, such as the expression of ICPs, the TMB, IPS, and the TIDE score. The results showed that patients in the high-risk group presented a higher response rate to immunotherapy, which was confirmed in several clinical cohorts treated with anti-PD1/anti-PD-L1 antibodies. Moreover, similar results were obtained when the sensitivity of the two groups to multiple chemotherapeutic drugs was predicted and validated: the patients in the high-risk group were more sensitive to most of the drugs. Moreover, at the single-cell level, we explored the expression patterns of TRGs and the cell-cell communication differences between the two groups of cells with different taurine metabolic activities. Surprisingly, it was the variation in the interaction between CD8 + T cells and other cells that accounted for most of the variation in intercellular communication, further suggesting a potential role for taurine in regulating the function of CD8 + T cells in the TME. Finally, we characterized the metabolic
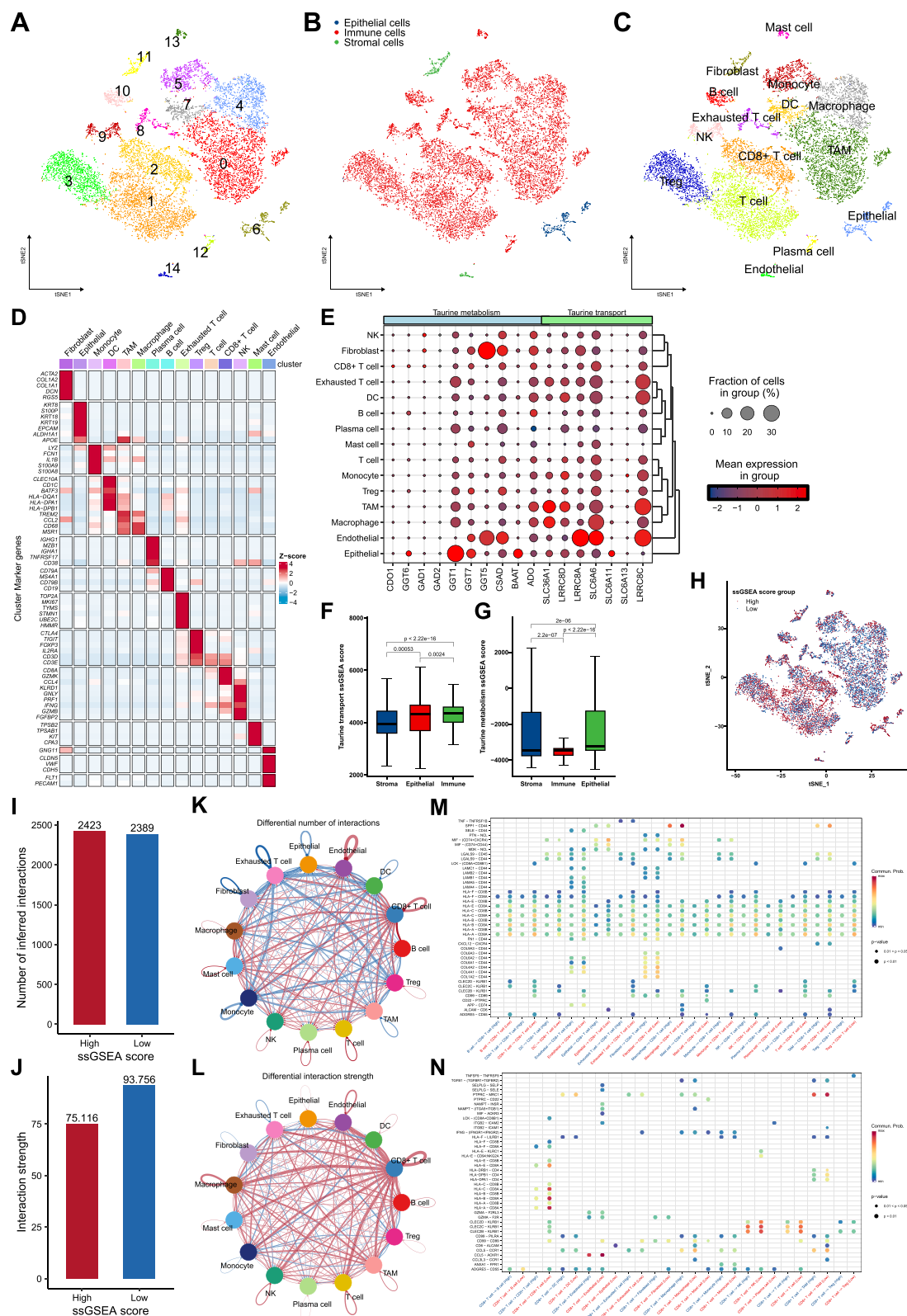
Fig. 10. Characteristic of taurine metabolism in the tumor microenvironment. (A) t-SNE plot of the 15 cell clusters. (B) Preliminary annotation of cell types through the expression of CD45 and EPCAM. (C) t-SNE plot of the 15 cell types annotated by marker genes. (D) Heatmap showing the expression of corresponding marker genes in the 15 cell types. (E) The expression pattern of TRGs in 15 cell types. (F and G) Comparison of the ssGSEA score of taurine transport and metabolism between three major cell types. (H) the t-SNE plot of the high and low groups according to the metabolic activity. (I and J) Comparison of the number (I) and strength (J) of ligand–receptor interactions between the high and low metabolic activity groups. (K and L) Differential number (K) and strength (L) of ligand–receptor interactions between the high and low metabolic activity groups. Red represents the low activity group had more and stronger interactions than the high group, otherwise blue. The line thickness was proportional to the number and strength of differential interactions. (M and N) Comparison of the ligand-receptor pairs in the communication of other cells to CD8 + T cells (C) and the communication of CD8 + T cells to other cells (D) between the high- and low-activity groups.
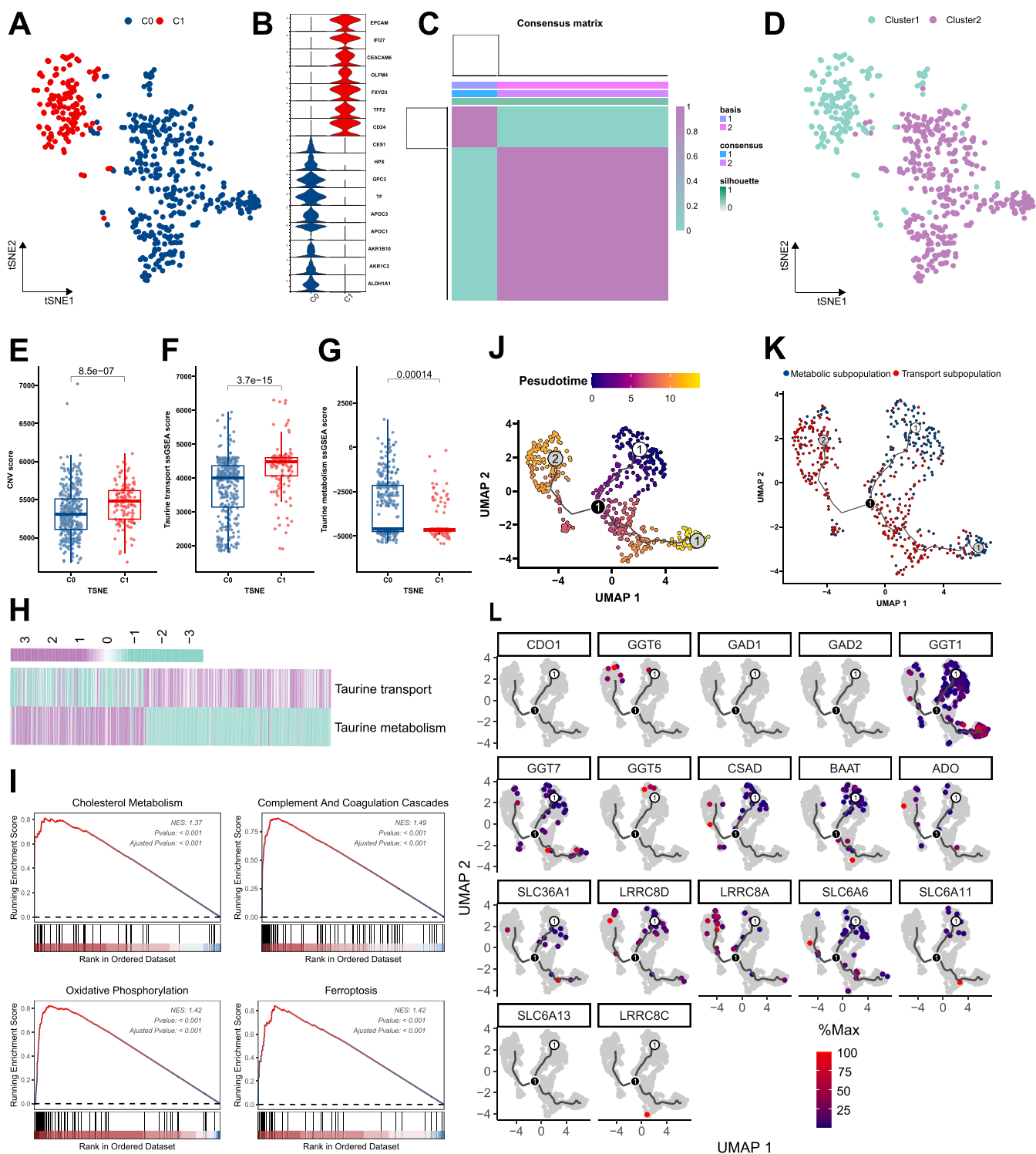
Fig. 11. Heterogeneity of taurine metabolism in epithelial cells. (A) t-SNE plot showing the subtypes of epithelial cells. (B) Stacked violin plots showing the marker genes for each epithelial cell subgroup. (C) The consensus matrix heatmap of the non-negative matrix factorization (NMF) clustering algorithm. (D) t-SNE plot showing the distribution of epithelial cells clustered by NMF algorithm. (E, F, G) Comparison of the CNV score (E), taurine transport (F), and metabolism (G) ssGSEA score in the two subtypes of epithelial cells. (H) Heatmap showing the ssGSEA score of taurine transport and metabolism gene sets in all epithelial cells. (I) Gene set enrichment analysis showing multiple pathways enriched in metabolism subpopulation. (J) Pseudo-time trajectory of epithelial cells as represented in the uniform manifold approximation and projection (UMAP) plot. (K) The trajectory manifold revealed the transcriptional state of taurine metabolism in epithelial cells. (L) The pseudo-time trajectory of transcriptional changes in TRGs.

heterogeneity of taurine in malignant cells in the TME and depicted the different transcriptional states of taurine metabolism in malignant cells using pseudo-time analysis.

The complex network of metabolic pathways in the TME has been shown to be involved in regulating the composition and function of various components of the TME, and therefore targeting metabolic pathways to enhance the efficacy of immunotherapy is a potentially promising therapeutic strategy [61]. Taurine is one of the most abundant free amino acids in mammalian tissues, and metabolomic analysis of over 900 tissue samples from a variety of cancers has shown that the taurine level is elevated across a variety of tumor tissues compared with that in normal tissues, and is involved in shaping the suppressive TME, along with acylcarnitine, lactate, and kynurenine [62]. However, the distribution of taurine in various cell types in the TME and how it is involved in the immune regulatory network remains unknown. Herein, the scRNA-seq analysis showed that cancer cells were the main users of taurine in the TME of patients with HCC. In addition, as the tumor progresses, cancer cells might meet their own metabolic demands by hijacking large amounts of taurine from the microenvironment. Furthermore, the cell communication results also showed that among various cells in the TME, the cell type most affected by this metabolic pattern of cancer cells was CD8 +T cells, the main enforcer of anti-tumor immunity, which further suggested that tumor cells might achieve immune escape by hijacking large amounts of taurine from the microenvironment and thereby affecting the function of CD8 +T cells. As Hung et al., demonstrated, cancer cells do this to methionine [57].

Another more important question is what role does taurine play in the process of anti-tumor immunity of CD8 + T cells? A recent study showed that taurine supplementation enhanced the anti-tumor capacity of CD8 + T cells cultured in vitro by reducing apoptosis and promoting the secretion of the cytokines IFN-γ and TNF-α, which are the key cytokines for anti-tumor immunity [63]. This suggested that a lack of sufficient taurine will impair the tumor-killing ability of CD8 + T cells. In addition, our analysis of cell-cell communication displayed that CD8 + T cells with high metabolic activity showed an impaired ability to accept antigens presented by other antigen-presenting cells because of the lower intracellular concentrations of available taurine compared with cells with a lower metabolic activity, which might also be one of the mechanisms by which tumor cells acquire the immune escape ability after reprogramming taurine metabolism. Notably, taurine also plays a significant role in other cells in the TME. The expression profiles of TRGs in the TME of HCC indicated that macrophages and TAMs also take up large amounts of taurine through the high expression of taurine transporters, and it was previously shown that taurine antagonizes the polarization of macrophages to M1 in the TME [15]. Our study showed that low taurine metabolic activity increased the strength of the interaction between CD8 +T cells and TAMs, as well as macrophages, via the SPP1-CD44 axis, the enhancement of this pathway promotes the polarization of macrophages toward the M2 phenotype [54]. Taken together, these results suggested that taurine uptake by macrophages in the TME might promote their polarization toward TAMs. In addition, the role of taurine in endothelial cells cannot be ignored. The rapid growth and distant metastasis of tumors depended on a large number of blood vessels to supply the required oxygen and nutrients, and the expression profiles showed that endothelial cells also transported and metabolized large amounts of taurine. Previous studies have revealed that taurine can exert vascular protective effects by reducing lipid peroxidation [64]; however, the role of taurine in tumor neovascularization requires further exploration.

Among the five hub genes used for TRPS construction, CSAD is considered to be the key rate-limiting enzyme for taurine synthesis in vivo. The results of the present study showed that the expression of *CSAD* mRNA was significantly decreased in tumor tissues compared with that in normal tissues, which was associated with worse patient prognosis. According to the calculation formula of the TRPS, the lower the expression of CSAD in patients, the higher the risk score and the

worse the prognosis, suggesting that taurine supplementation might improve the prognosis of patients with HCC, although this needs to be confirmed by further experiments. A recent study showed that plasma taurine levels were higher in patients with lung cancer who responded to PD-1 blockade antibody therapy than in non-responders, and taurine supplementation improved the sensitivity to ICB therapy in subcutaneous tumor-bearing mice [63]. In addition, our study showed that patients with a higher TRPS were more likely to benefit from immunotherapy, as confirmed in several clinical cohorts treated with anti-PD1/anti-PD-L1 antibodies. These results suggested that plasma or intra-tumor levels of taurine can influence the efficacy of immunotherapy. However, it is important to note that, because of differences in the TME, further metabolomics data from a prospective cohort are needed in HCC to characterize plasma and intratumor taurine levels in patients with different TRPS and to investigate the effect of taurine on immunotherapy.

Despite some new insights into the role of taurine metabolism in HCC provided by our findings, this study has several limitations. Firstly, the construction and validation of the risk model were based on public databases. Therefore, the performance of the TRPS needs to be further evaluated using prospective clinical research. Secondly, because of the lack of in vivo and in vitro experiments, the elusive mechanisms of taurine metabolism involved in the immune regulatory network in the TME remain to be determined. Finally, limited computational resources meant that we only considered the heterogeneity within the malignant cells and did not consider interpatient heterogeneity.

In conclusion, we identified two heterogeneous subtypes of taurine metabolism in patients with HCC that presented significantly different genomic features, clinicopathological characteristics, and immune cell infiltration. In addition, we constructed a risk model, termed TRPS, based on five hub TRGs that can be used as predictors of prognosis, immunotherapy response, and chemotherapy response in patients with HCC. Finally, we explored the expression pattern of TRGs and the heterogeneity of taurine metabolism within cancer cells at the single-cell level. This study facilitated a deeper understanding of taurine metabolism in HCC and will guide more precise clinical management and treatment.

5. Conclusions

Two heterogeneous subtypes of taurine metabolism that presented significantly different genomic features, clinicopathological characteristics, and immune cell infiltration were identified in patients with HCC. The risk model TRPS was not only an independent factor for the clinical prognosis of patients but also achieved relatively high performance in short- and long-term survival prediction. In addition, a higher TRPS score implies a higher response rate to immunotherapy and chemotherapy.

Statements and declarations

Ethics approval and consent to participate.

As no human subjects were recruited for this study, obtaining consent is not applicable.

CRediT authorship contribution statement

X.B. and T.L. conceived this study. Q.L., Y.L., X.Z. collected the literature. Q.L., Y.L., X.Z. performed the bioinformatics analysis, data interpretation, and prepared the figures. Q.L., Y.L., X.Z. wrote the manuscript. H.Y., Y.C., and H.Z. helped with the manuscript and data review. All authors read and approved the final manuscript. Q.L., Y.L., X. Z. contributed equally to the drafting process. X.B. and T.L. share senior authorship.

Consent for publication

Not applicable.

Declaration of Competing Interest

The authors declare that they have no conflict of interest.

Availability of data and materials

The datasets supporting the conclusions of this article are available in the TCGA database (http://cancergenome.nih.gov/), the GEO database (https://www.ncbi.nlm.nih.gov/), the ICGC database (https://dcc.icgc.org/), and the TIGER database (http://tiger.canceromics.org/).

Acknowledgments

Not applicable.

Appendix A. Supporting information

Supplementary data associated with this article can be found in the online version at doi:10.1016/j.csbj.2023.11.014.

References

[1] Villanueva A. Hepatocellular carcinoma. N Engl J Med 2019;380(15):1450–62.
[2] Sung H, et al. Global Cancer Statistics 2020: GLOBOCAN estimates of incidence and mortality worldwide for 36 cancers in 185 countries. CA Cancer J Clin 2021;71(3):209–49.
[3] Ringelhan M, et al. The immunology of hepatocellular carcinoma. Nat Immunol 2018;19(3):222–32.
[4] Chen L, Han X. Anti-PD-1/PD-L1 therapy of human cancer: past, present, and future. J Clin Invest 2015;125(9):3384–91.
[5] Wolchok JD, et al. Nivolumab plus ipilimumab in advanced melanoma. N Engl J Med 2013;369(2):122–33.
[6] Pfister D, et al. NASH limits anti-tumour surveillance in immunotherapy-treated HCC. Nature 2021;592(7854):450–6.
[7] Hanahan D. Hallmarks of cancer: new dimensions. Cancer Discov 2022;12(1):31–46.
[8] Bader JE, Voss K, Rathmell JC. Targeting metabolism to improve the tumor microenvironment for cancer immunotherapy. Mol Cell 2020;78(6):1019–33.
[9] Huxtable RJ. Physiological actions of taurine. Physiol Rev 1992;72(1):101–63.
[10] Chen C, et al. Roles of taurine in cognitive function of physiology, pathologies and toxication. Life Sci 2019;231:116584.
[11] Seidel U, Huebbe P, Rimbach G. Taurine: a regulator of cellular redox homeostasis and skeletal muscle function. Mol Nutr Food Res 2019;63(16):e1800569 (p).
[12] Ma N, et al. Taurine and its anticancer functions: in vivo and in vitro study. Adv Exp Med Biol 2022;1370:121–8.
[13] Nishio S, et al. The effect of taurine on age-related immune decline in mice: the effect of taurine on T cell and B cell proliferative response under costimulation with ionomycin and phorbol myristate acetate. Mech Ageing Dev 1990;52(2–3):125–39.
[14] Maher SG, et al. Taurine attenuates CD3/interleukin-2-induced T cell apoptosis in an in vitro model of activation-induced cell death *(AICD)*. Clin Exp Immunol 2005;139(2):279–86.
[15] Meng L, et al. Taurine antagonizes macrophages M1 polarization by mitophagy-glycolysis switch blockage via dragging SAM-PP2Ac transmethylation. Front Immunol 2021;12:648913.
[16] Ping Y, et al. Taurine enhances the antitumor efficacy of PD-1 antibody by boosting CD8(+) T cell function. Cancer Immunol Immunother 2023;72(4):1015–27.
[17] Wang W, et al. Dysregulated serum metabolites in staging of hepatocellular carcinoma. Clin Biochem 2018;61:7–11.
[18] El Agouza IM, et al. Taurine: a novel tumor marker for enhanced detection of breast cancer among female patients. Angiogenesis 2011;14(3):321–30.
[19] Tomczak K, Czerwinska P, Wiznerowicz M. The Cancer Genome Atlas (TCGA): an immeasurable source of knowledge. Conte Oncol (Pozn) 2015;19(1A):A68–77.
[20] Zhang J, et al. The international cancer genome consortium data portal. Nat Biotechnol 2019;37(4):367–9.
[21] Barrett T, et al. NCBI GEO: archive for functional genomics data sets–update. Nucleic Acids Res 2013;41(Database issue):D991–5.
[22] Mariathasan S, et al. TGFbeta attenuates tumour response to PD-L1 blockade by contributing to exclusion of T cells. Nature 2018;554(7693):544–8.
[23] Chen Z, et al. TIGER: a web portal of tumor immunotherapy gene expression resource. Genom Proteom Bioinforma 2022.
[24] Leek JT, et al. The sva package for removing batch effects and other unwanted variation in high-throughput experiments. Bioinformatics 2012;28(6):882–3.
[25] Mayakonda A, et al. Maftools: efficient and comprehensive analysis of somatic variants in cancer. Genome Res 2018;28(11):1747–56.
[26] Wilkerson MD, Hayes DN. ConsensusClusterPlus: a class discovery tool with confidence assessments and item tracking. Bioinformatics 2010;26(12):1572–3.
[27] Hanzelmann S, Castelo R, Guinney J. GSVA: gene set variation analysis for microarray and RNA-seq data. BMC Bioinforma 2013;14:7.
[28] Liao Y, et al. WebGestalt 2019: gene set analysis toolkit with revamped UIs and APIs. Nucleic Acids Res 2019;47(W1):W199–205.
[29] Yu G, et al. clusterProfiler: an R package for comparing biological themes among gene clusters. OMICS 2012;16(5):284–7.
[30] Liberzon A, et al. The molecular signatures database (MSigDB) hallmark gene set collection. Cell Syst 2015;1(6):417–25.
[31] Sanchez-Vega F, et al. Oncogenic signaling pathways in the cancer genome atlas. Cell 2018;173(2):321–37. e10.
[32] Kumar A, et al. Substantial interindividual and limited intraindividual genomic diversity among tumors from men with metastatic prostate cancer. Nat Med 2016;22(4):369–78.
[33] Zeng D, et al. IOBR: multi-omics immuno-oncology biological research to decode tumor microenvironment and signatures. Front Immunol 2021;12:687975.
[34] Becht E, et al. Estimating the population abundance of tissue-infiltrating immune and stromal cell populations using gene expression. Genome Biol 2016;17(1):218.
[35] Yoshihara K, et al. Inferring tumour purity and stromal and immune cell admixture from expression data. Nat Commun 2013;4:2612.
[36] Thorsson V, et al. The immune landscape of cancer. Immunity 2018;48(4):812–30. e14.
[37] Gui J, Li H. Penalized Cox regression analysis in the high-dimensional and low-sample size settings, with applications to microarray gene expression data. Bioinformatics 2005;21(13):3001–8.
[38] Robin X, et al. pROC: an open-source package for R and S+ to analyze and compare ROC curves. BMC Bioinforma 2011;12:77.
[39] Charoentong P, et al. Pan-cancer Immunogenomic Analyses Reveal Genotype-Immunophenotype Relationships and Predictors of Response to Checkpoint Blockade. Cell Rep 2017;18(1):248–62.
[40] Samstein RM, et al. Tumor mutational load predicts survival after immunotherapy across multiple cancer types. Nat Genet 2019;51(2):202–6.
[41] Jiang P, et al. Signatures of T cell dysfunction and exclusion predict cancer immunotherapy response. Nat Med 2018;24(10):1550–8.
[42] Geeleher P, Cox N, Huang RS. pRRophetic: an R package for prediction of clinical chemotherapeutic response from tumor gene expression levels. PLoS One 2014;9(9):e107468.
[43] Geeleher P, Cox NJ, Huang RS. Clinical drug response can be predicted using baseline gene expression levels and in vitro drug sensitivity in cell lines. Genome Biol 2014;15(3):R47.
[44] Butler A, et al. Integrating single-cell transcriptomic data across different conditions, technologies, and species. Nat Biotechnol 2018;36(5):411–20.
[45] Hu C, et al. CellMarker 2.0: an updated database of manually curated cell markers in human/mouse and web tools based on scRNA-seq data. Nucleic Acids Res 2023;51(D1):D870–6.
[46] Jin S, et al. Inference and analysis of cell-cell communication using CellChat. Nat Commun 2021;12(1):1088.
[47] Patel AP, et al. Single-cell RNA-seq highlights intratumoral heterogeneity in primary glioblastoma. Science 2014;344(6190):1396–401.
[48] Trapnell C, et al. The dynamics and regulators of cell fate decisions are revealed by pseudotemporal ordering of single cells. Nat Biotechnol 2014;32(4):381–6.
[49] Jin N, et al. Identification of metabolic vulnerabilities of receptor tyrosine kinases-driven cancer. Nat Commun 2019;10(1):2701.
[50] Xia Y, et al. Metabolic reprogramming by MYCN confers dependence on the serine-glycine-one-carbon biosynthetic pathway. Cancer Res 2019;79(15):3837–50.
[51] Calderaro J, et al. Molecular and histological correlations in liver cancer. J Hepatol 2019;71(3):616–30.
[52] Llovet JM, et al. Hepatocellular carcinoma. Nat Rev Dis Prim 2021;7(1):6.
[53] Rebouissou S, Nault JC. Advances in molecular classification and precision oncology in hepatocellular carcinoma. J Hepatol 2020;72(2):215–29.
[54] Liu L, et al. Construction of TME and Identification of crosstalk between malignant cells and macrophages by SPP1 in hepatocellular carcinoma. Cancer Immunol Immunother 2022;71(1):121–36.
[55] Liu Y, et al. Single-cell transcriptomic analysis reveals macrophage-tumor crosstalk in hepatocellular carcinoma. Front Immunol 2022;13:955390.
[56] Groblewska M, Litman-Zawadzka A, Mroczko B. The role of selected chemokines and their receptors in the development of gliomas. Int J Mol Sci 2020;21(10).
[57] Hung MH, et al. Tumor methionine metabolism drives T-cell exhaustion in hepatocellular carcinoma. Nat Commun 2021;12(1):1455.
[58] Kraehenbuehl L, et al. Enhancing immunotherapy in cancer by targeting emerging immunomodulatory pathways. Nat Rev Clin Oncol 2022;19(1):37–50.

[59] Siu LL, et al. Challenges and opportunities in adapting clinical trial design for immunotherapies. Clin Cancer Res 2017;23(17):4950–8.

[60] Haslam A, Prasad V. Estimation of the percentage of US patients with cancer who are eligible for and respond to checkpoint inhibitor immunotherapy drugs. JAMA Netw Open 2019;2(5):e192535.

[61] Guerra L, Bonetti L, Brenner D. Metabolic modulation of immunity: a new concept in cancer immunotherapy. Cell Rep 2020;32(1):107848.

[62] Reznik E, et al. A landscape of metabolic variation across tumor types. Cell Syst 2018;6(3):301–13. e3.

[63] Ping Y, et al. Taurine enhances the antitumor efficacy of PD-1 antibody by boosting CD8(+) T cell function. Cancer Immunol Immunother 2022.

[64] Leao VF, et al. Taurine supplementation prevents endothelial dysfunction and attenuates structural changes in aortas from hypothalamic obese rats. Eur J Nutr 2019;58(2):551–63.